Master's Thesis
석사 학위논문

Development of a Low-Noise Wideband Signal Receiver for Combined PA and US Imaging

Wonkook Han(한 원 국 韓 沅 陽)

Department of Information and Communication Engineering
정보통신융합전공

DGIST

2021

Development of a Low-Noise Wideband Signal Receiver for Combined PA and US Imaging

Advisor: Professor Jin Ho Chang
Co-advisor: Professor Jae Youn Hwang

by

Wonkook Han
Department of Information Communication Engineering
DGIST

A thesis submitted to the faculty of DGIST in partial fulfillment of the requirements for the degree of Master of Science in the Department of Information and Communication Engineering. The study was conducted in accordance with Code of Research Ethics[1]

07. 08. 2021

Approved by

Professor Jin Ho Chang (signature)
(Advisor)

Professor Jae Youn Hwang (signature)
(Co-Advisor)

[1] Declaration of Ethical Conduct in Research: I, as a graduate student of DGIST, hereby declare that I have not committed any acts that may damage the credibility of my research. These include, but are not limited to: falsification, thesis written by someone else, distortion of research findings or plagiarism. I affirm that my thesis contains honest conclusions based on my own careful research under the guidance of my thesis advisor.

Development of a Low-Noise Wideband Signal Receiver for Combined PA and US Imaging

Wonkook Han

Accepted in partial fulfillment of the requirements for the degree of Master of Science.

07. 08. 2021

Head of Committee Prof. Jin Ho Chang (signature)

Committee Member Prof. Jae Youn Hwang (signature)

Committee Member Prof. Junghyup Lee (signature)

MS/ES
202022028

한 원 국. Wonkook Han. Development of a Low-Noise Wideband Signal Receiver for Combined PA and US Imaging. Department of Information Communication Engineering. 2021. 36p. Advisors Prof. Jin Ho Chang, Co-Advisors Prof. Jae Youn Hwang

ABSTRACT

Multimodal imaging based on ultrasound (US) and photoacoustic (PA) can provide high spatial and contrast resolution images, thus improving the diagnosis accuracy of certain cell diseases, such as cancer. In general, a commercial US system is used to receive the PA signal. However, due to the limitation of spectral bandwidth of the commercial receivers, photoacoustic microscopy (PAM) imaging that gives information on anatomical and functional structure requires the combination of several pieces of commercially available equipment. Potential problems such as attenuation and noise increase of PA signals due to the impedance mismatch between devices, synchronization problems due to inaccurate trigger timing, and lack of analog time-gain-compensation functionality depending on imaging depth can lead to degradation of signal-to-noise-ratio (SNR) and contrast-to-noise-ratio (CNR) performance. To solve these issues, and optimized low-noise wideband reception system for combined PA and US imaging was developed. the main module of this system is a low noise, a wideband signal receiver that consists of two low-noise amplifiers (LNA), two variable gain amplifiers (VGA), analog filters, an analog-to-digital converter (ADC), and control logic. From tissue-mimicking phantom, blood vessel phantom, and wire target imaging experiments, it was found that the developed system can improve SNR by 6.7 dB and CNR by 3 dB, compared to a combination of several pieces of commercially available equipment.

Keywords: photoacoustic microscopy; contrast-to-noise-ratio; signal-to-noise-ratio; variable gain amplification; low noise gain amplification

List of Contents

List of Tables

List of Figures

I. INTRODUCTION

The development of medical technology and medical equipment has increased human lifespan, and interest in medical imaging equipment has increased. Recently, there is increasing research on fusion images that combine different medical images such as X-ray, MRI, CT, PET, and ultrasound (US) to overcome the shortcomings of the device and maximize its advantages. Including SPECT/CT and PET/CT that integrate anatomical images and functional images, PET/MR, which is a fusion of anatomical images of human tissues, MRI capable of metabolic and functional analysis, and PET capable of examining the activity and metabolic state of human cells to the molecular level, is an example of medical combined imaging technology [1].

Medical US images are harmless to the human body and do not use radiation that is harmful to the human body, and high-resolution images can be obtained in real-time, so it is possible to observe not only the internal organ structure of the human body, and there is an advantage that the blood flow inside the blood vessel can also be measured [2–4]. On the other hand, US waves do not penetrate bones and air, so it is difficult to obtain images of structures composed of bones and air [4], and they have the disadvantage of lower contrast than X-ray, CT, and MRI imaging devices. In particular, low contrast images have limitations on disease and lesion diagnosis.

Photoacoustic microscopy (PAM) images, which is one of the Photoacoustic (PA) images application fields, an acoustic signal is generated in the thermal expansion process by focusing the laser beam on target molecules and absorbing the laser energy irradiated by the molecules [5]. Acoustic signals generated at this time have US frequency bands, and PA signals can be received using an US transducer to obtain spatial resolution and high-resolution images [6]. On the other hand, various biological tissues inside the human body have different laser energy absorption coefficients depending on the wavelength of a particular laser [5]. Thus, the disadvantage is that depending on the wavelength of the laser, only information about certain biological tissues can be obtained and geometric information cannot be obtained inside the human body. Therefore, research on high-resolution US and PAM image integrated reception systems that can obtain these US images and PAM images at the same time and simultaneously secure the advantages while overcoming the problems of each image is being actively conducted.

In generally, the performance evaluation of an US image is determined by the signal-to-noise ratio (SNR) and the Contrast-to-Noise Ratio (CNR). That is, maintaining an excellent SNR and CNR is of utmost importance in

US images. The resolution of US images increases as the transmission frequency and frequency bandwidth increase. However, the amount of attenuation that increases in proportion to frequency causes a decrease in penetration depth. In other words, to obtain high-resolution US images, a system that can effectively receive signals with high frequencies and wide frequency bandwidth is required.

PAM images, a combination of several pieces of commercially available equipment, so they cannot be obtained simultaneously with US images, and there is a problem that the combination of commercial devices is not suitable for high-resolution PAM images. To obtain high-resolution PAM images, low-noise amplifiers (LNA) that generally increase the amplitude of the PA signal, a variable gain amplifier (VGA) that compensates for attenuation according to the penetration depth, an analog filter to remove unnecessary noise signals, and the receiving system must be equipped with an electrical impedance matching circuit to pass the PA signal received by the transducer to the receiving system with the minimal loss [7] However, typical PAM receiving systems only use commercial LNA, digitizers, and trigger signal generators. [8] Also, there is no electrical impedance matching circuit between commercial equipment. Unnecessary signal attenuation and noise may limit high-resolution PAM images. In addition, combining commercial equipment in a typical PAM system increases the volume of the system and limits application fields. Therefore, simultaneous acquisition of high-resolution US and PAM images requires the receiving system to simultaneously meet both low noise and wideband characteristics, and it is important to implement a single system for system integration.

In the thesis, report a recently developed imaging system for combined PA and US that consists of a hybrid sensor based on an optically transparent transducer [9], a laser system, a motorized stage and controller, a signal receiving module, and a host computer. The signal receiving module is composed of two LNAs, two VGAs, analog filters, an analog-to-digital converter (ADC), and control logic. Considering a low signal amplitude, the receiving module was specially developed to provide an amplification gain as large as possible, but noise as low as possible. For this, the unique arrangement of two LNAs and two VGAs was employed. Since PA signals generally have a wide spectral bandwidth [6], the receiving module was designed to have a wide operating bandwidth with a small magnitude fluctuation. The imaging performance of the developed system was evaluated through in vitro experiments in terms of SNR and CNR improvement.

II. STRUCTURE OF THE PROPOSED RECEIVE SYSTEM

2.1 Description of the developed receive system

The proposed receiving system requires amplification gains of more than 20 dB to sufficiently amplify the low-reception sensitivity signal of the high-frequency transducer used to receive wide spectrum signals of PA signals. In addition, to compensate the attenuation according to the high frequency and penetration depth, to satisfy the variable gain range of 40 dB or more, and to prevent the reception signal distortion by the amplifier, the design goals of the receiving system are shown in Table 2.1.

Table 2.1. Design goals of the proposed receive system.

Maximum operating frequency (MHz)	> 70
Minimum amplification gain (dB)	> 76
Amplification gain flatness (dB)	< ±1
Amplification gain range (dB)	> 48

The signal receiving module is composed of an analog frontend block, an analog time gain compensation (ATGC) block, a high-voltage pulser block, and a digital control block, as shown in Figure. 2.1. Considering the input voltage range of an ADC, the maximum amplification gain was determined to be higher than 70 dB at an operating frequency range of 5 to 70 MHz. Also, high gain flatness should be achieved for the minimal distortion of receive signals, so that the design goal of the gain flatness was less than ±1 dB. Note that OR-PAM (Optical Resolution-Photoacoustic Microscopy) uses low frequency transducers because spatial resolution is determined by laser beam size, whereas AR-PAM (Acoustic Resolution-Photoacoustic Microscopy) employs high frequency transducers because the spatial resolution is linearly proportional to the frequency of transducers [10,11]. In addition, general medical US images use high-frequency transducer to improve spatial resolution. The requirements are difficult to be met with the typical configuration of signal amplification block that contains one LNA and one VGA. In addition, amplifiers with a high gain generally produce high amplitude noise. To tackle these challenges, came up with the unique arrangement of LNAs and VGAs, i.e., alternatively arrangement of two LNAs and two VGA to avoid signal saturation through the amplification block (see the block diagram of the analog frontend in Figure. 2.1).

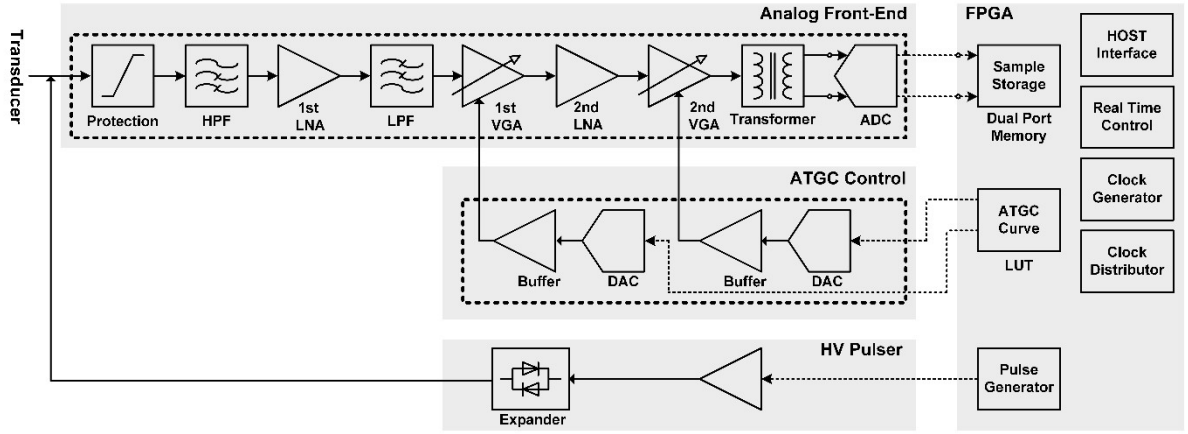

Figure 2.1. Conceptual block diagram of the proposed developed signal receiving module.

Acoustic signals received by a transducer contains white noise and low frequency noise [12]. After the system protection circuit composed of three diodes, an analog band pass filter (BPF) was placed to remove the noise, thus increasing SNR. The BPF was implemented using one analog high pass filter (HPF) with a cutoff frequency of 5 MHz and one low pass filter (LPF) with a cutoff frequency of 70 MHz. The output signals of the BPF were increased in the first LNA and VGA block. The LNA (AD8000, Analog Device Inc., Norwood, MA, USA) had a low input voltage noise of 1.6 nV/√Hz and an amplification gain of 20 dB. The VGA (AD8337, Analog Device Inc., Norwood, MA, USA) had an adjustable amplification gain of -6 to 18 dB. Therefore, the amplification gain in this block can be changed from 14 to 38 dB, depending on the acoustic signal amplitude received by a transducer. Since the output signals of LNAs and VGAs generally contain the harmonics of the original signal, the harmonics should be removed before another amplification. For this, the same LPF was placed in front of the second LNA and VGA block. As a result, the signal receiving module had the ability to increase PA and US signal amplitude to 76 dB at maximum. The VGA gains can be adjusted by changing the gain control voltage in the ATGC control block. For OR-PAM, the VGA gains prefer constant, and the values are determined by the amplitude of the original PA signals to avoid signal saturation after amplification as well as to use the full input voltage range of ADC. For AR-PAM and US images providing a relatively deep imaging depth, the VGAs can be used for compensating for signal loss due to the frequency-dependent attenuation and diffraction of PA signals; the loss occurs exponentially as a function of imaging depth. For this, ATGC curves are designed to exponentially increase received signals as a function of imaging depth and stored in FPGA (Field Programmable Gate Array) in the digital control block. According to the ATGC curves, the two VGA gains are adjusted by changing their gain control voltages that are produced in two DACs (AD5424, Analog Devices Inc., Norwood, MA). The output signal of the second amplification block is transferred to ADC (AD9626, Analog Device Inc., Norwood, MA, USA) after changing a single-ended signal to differential signals by using two 1:1

RF transmission line transformers (ETC1-1-13, MACOM, Lowell, MA, USA). By doing so, the effect of electromagnetic interference (EMI) and cross-talk noises can be minimized, thus maintaining the SNR of the amplified receive signals. In the ADC, the received signals are digitized to 12 bits at a rate of 250 MHz, and the data are stored into the internal memory of FPGA (XC6SLX75, Xilinx Inc., San Jose, CA, USA), as shown in Figure 2.2. The main role of the digital control block is to transfer the digitized samples to the Host PC and control the ATGC block and the ADC.

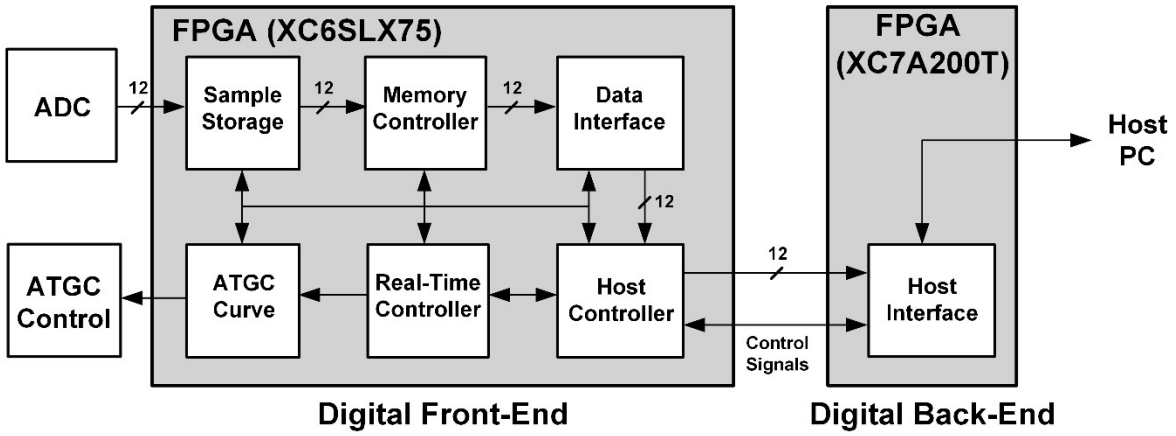

Figure 2.2. Block diagram of the digital control block designed and implemented in FPGA.

III. IMPLEMENTATION OF PROPOSED RECEIVE SYSTEM

3.1 Implementation of the signal receiving module

The designed signal receiving module was implemented on the printed circuit board (PCB), as shown in Figure. 3.1(a); the PCB consisted of 9 signal layers and 7 ground layers. The PCB was made of FR-4 material with a thickness of 2.4 mm, and the analog and digital regions were separated to minimize the digital signal interference to the analog signals. The total board size was 270 mm x 260 mm. The dimension of the transmission line was determined so that the characteristic impedance of all the transmission lines was 50 Ω. The electrical impedance matching is particularly important when a PCB deal with small signals such as PA signals [13]. Especially, the analog region was shielded with metal-shield-caps that were capable of EMI shielding and thus minimizing the effects of external noise on the analog signals in the board. The metal shield cap was designed so that cavity resonance did not occur below a few hundred MHz, based on calculation of a cavity resonant frequency (see Figure. 3.1(a) and (b)). To communicate between the signal receiving module and the Host PC, as shown in Figure. 3.1(c), an Opal Kelly evaluation board (XEM7310MT-A200, Opal Kelly Inc., Portland, OR) was integrated into the PCB of the signal receiving module.

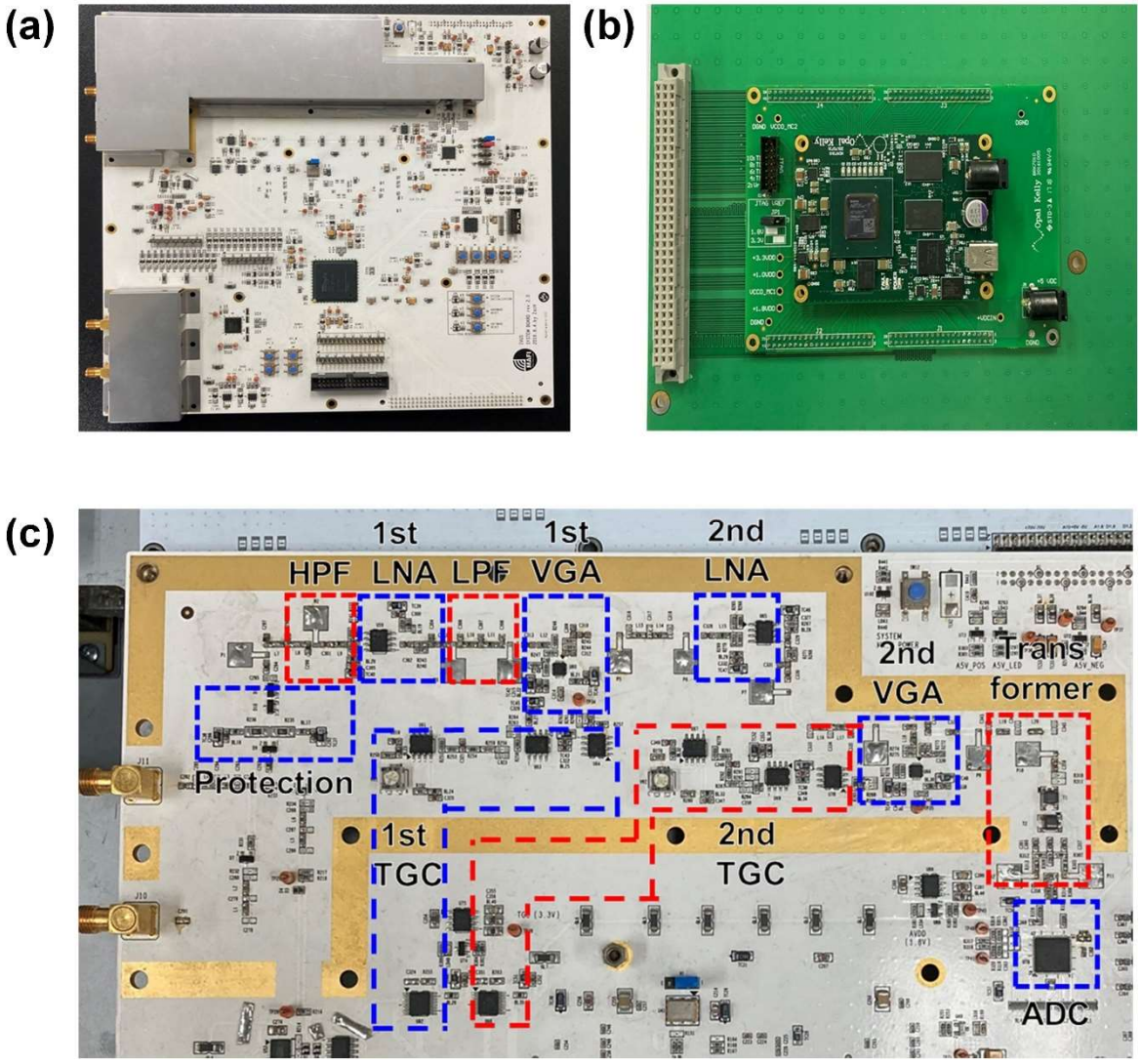

Figure 3.1. Photographs of the developed printed circuit boards of **(a)** the signal receiving module and **(b)** the Host PC communication board. The part of the analog frontend and the ATGC control blocks implemented in the PCB for the signal receiving module is magnified in **(c)**.

The developed low noise wideband receiving system was manufactured as shown in Figure 3.1. The Analog Front-end module amplifies the acoustic signal received through the US transducer to the desired level, suppression of the signal in the unnecessary frequency band, and transmits the analog received signal to the ADC to convert it into a digital signal. ADC module has the function of converting the received acoustic signal into a digital signal and transferring it to the FPGA. The System Clock module is a module that generates a system clock for synchronizing the operations of the electronic elements inserted in the receiving system board. FPGA & Configuration module is a module that performs the roles of ADC operation control, transmission/receive system control, and images data storage. The bipolar pulser module is the part that produces the high-voltage signal used in common US images. A system-to-PC communication module is a module that executes image system control, transfer of received images data, determination of transmission form, etc. via communication with the Host PC.

A system power module is a system power interface module that smoothly supplies the various levels of voltage required for the operation of the system board.

In addition, the developed analog front-end receiver module minimizes the return loss and distortion of the signal generated in the transmission line circuit through impedance matching of electrical characteristics [14]. At this time, the impedance matching value was matched to 50 Ω, an intermediate value between 30 Ω, which has the best power transmission efficiency, and 77 Ω, which has the least distortion of the received signal. Figure 3.2 shows the impedance characteristics of the developed Analog Front-End. The without matching describes the electrical characteristics of analog circuits during impedance mismatching between source and load. As a result, the received signal is lost due to non-uniform amplification and high return loss in the operating frequency band. With matching, a certain amplification performance is met in the operating frequency band through impedance matching between the source and the load. The input return loss (S11 Parameter) is optimized below -20 dB (i.e., This means that the return loss at the input port of the received signal is less than 1%) and the output return loss (S22 Parameter) is optimized below -13dB (i.e., This means that the return loss at the input port of the received signal is less than 5%) to minimize signal loss due to impedance mismatching.

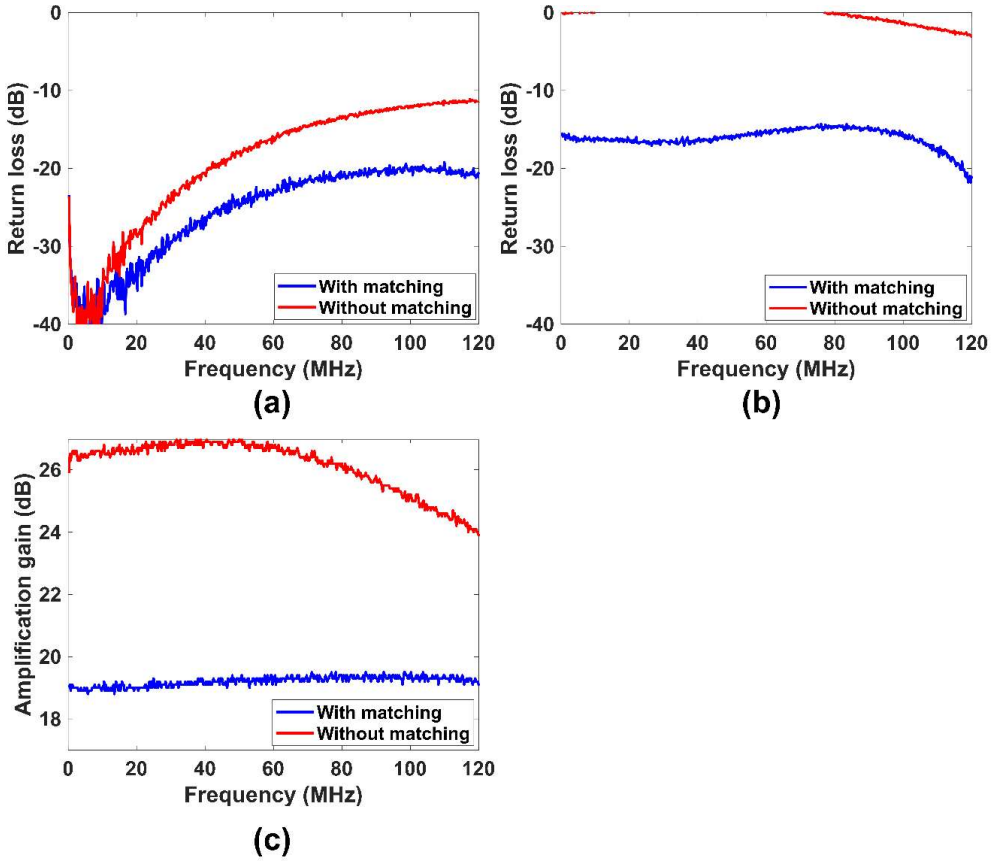

Figure 3.2. Transmission and reflection characteristics of the developed system. **(a)** Comparison of input return loss characteristics of developed systems through impedance matching. And **(b)** output return loss. **(c)** Comparison of insertion loss characteristics of developed systems through impedance matching.

3.2 Digital front-end module

The FPGA used to implement the Digital front-end module is the Spartan-6 XC6SLX75 Device, a type of Xilinx 6-Series. The 6-Series FPGA logic synthesis tool used ISE 14.4 in an Operating System (OS) Windows 10 (64 bit) environment. The Digital front-end module is configured to create a Real-time-control (RTC) signal for controlling the entire system and access it from the Host PC to control the registers in real-time. The amplification degree of the received signal, which is attenuated proportionally according to the depth, is adjusted. Then, the operation of the ADC chip that digitizes the analog data is controlled, the digitized data is received, and the data is transmitted to the Digital back-end module via the parallel interface. It will also generate a Bipolar pulser control signal for general US images.

RTC logic generates a pulse repetition frequency (PRF) signal for system driving when a system enable signal is applied through the host PC (Generally, in an US image system, PRF is the reference time for images transmission, and reception.). At this time, the low and high periods of the PRF signal are the time via the value in the register updated via the data path. At this time, the PRF signal is generated using the external trigger signal linked with the Nd: YAG laser system when acquiring the PA image. In this case, to satisfy the thermal expansion effect, the PRF low interval is set to 10 ns by the pulsed laser applied in a short time, and the PRF signal is generated.

Table 3.1. Developed system register map definition.

Register name	R/W	Address	Default	Description
PRF_START	R/W	0x100	0x0001	PRF generated signal
PRF_MODE	R/W	0x101	0x0001	External or internal PRF mode
PRF_LOW	R/W	0x102	0x0010	PRF low duration
PRF_HIGH	R/W	0x103	0xC350	PRF high duration
LASER_DELAY	R/W	0x200	0x0001	External trigger delay
SCANLINE_NUMBER	R	0x300		Current scanline position
SCAN_DEPTH	R/W	0x301	0x1A90	Image area of interest (Depth)
TX_FREQ	R/W	0x500	0x0002	Bipolar pulser width (Conventional US)
TX_ENABLE	R/W	0x501	0x0001	Bipolar pulser enable (Conventional US)
RX_WEIGHT	R/W	0x700	0x0000	Receive signal latency
ATGC_EN	R/W	0x600	0x0001	VGA Enable
ATGC_CURVE	R/W	0x601	0xCCCC	VGA increment curve
ADC_MODE	R/W	0x800	0x0D00	ADC mode setting
ADC_UPDATE	R/W	0x801	0x0000	ADC mode update
TRANS_MODE	R/W	0x900	0x0000	Test pattern data generation (Only debugging)

The developed system can utilize the DAC output voltage to adjust the VGA amplification to compensate for the magnitude of the received signal that is proportionally attenuated according to the depth of the image. The circuit schematic was constructed as follows Figure 3.3.

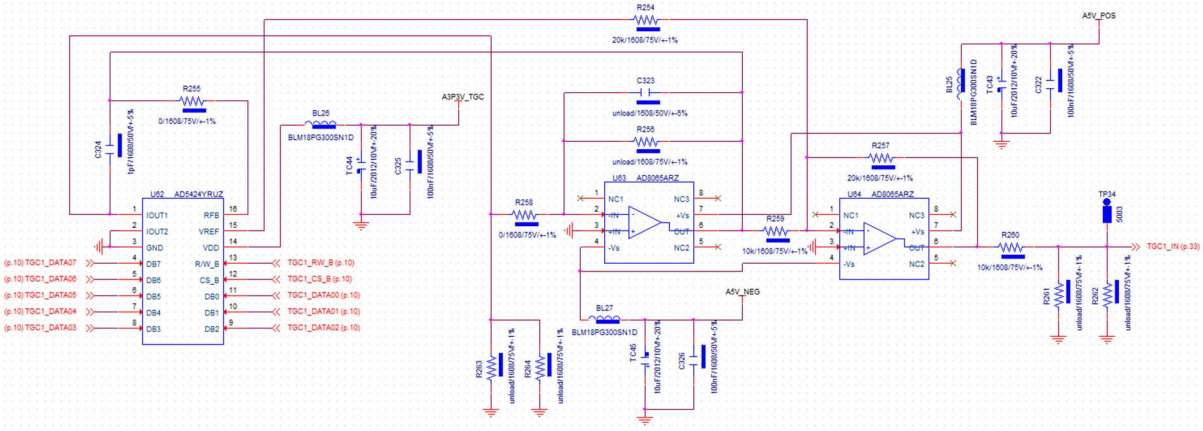

Figure 3.3. Schematic configuration for implementing DAC function

The maximum output voltage of the DAC is 1.2 V_{P-P}, and the range of the output voltage is adjusted via the input digital data 8 bit. The VGA amplification can be adjusted in 255 steps from -6 dB to 18 dB, and the timing and parameters for controlling the DAC output voltage are shown in Figure 3.4 and Table 3.2. The developed system was designed to allow the VGA amplification to be adjusted in images depth increments of 150 um. As shown in Figure 3.5, the DAC output voltage is synchronized with the PRF signal, and the curve of the DAC output voltage is determined by the system register.

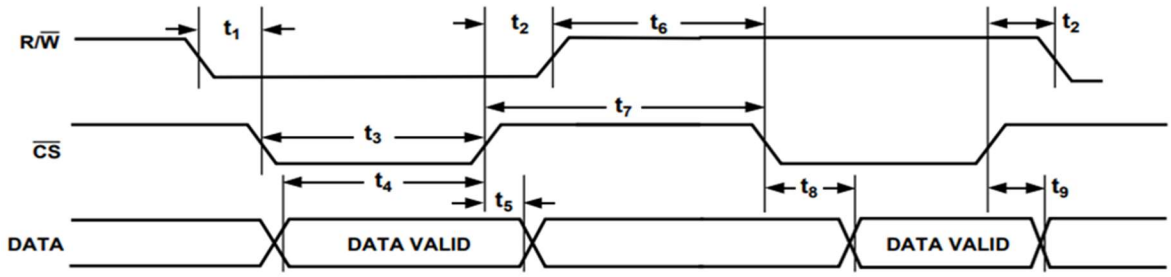

Figure 3.4. DAC Parallel Port Interface Timing Diagram.

Table 3.2. DAC parallel port interface timing parameter.

Parameter	Timing (ns)	Description
t_1		R/W to CS setup time
t_2		R/W to CS hold time
t_3	10	CS low time (write cycle)
t_4	6	Data setup time
t_5		Data hold time
t_6	5	R/W high to CS low
t_7	7	CS min high time
t_8	10 (Typically) 20 (Max)	Data access time
t_9	5 (Typically) 10 (Max)	Bus relinquish time

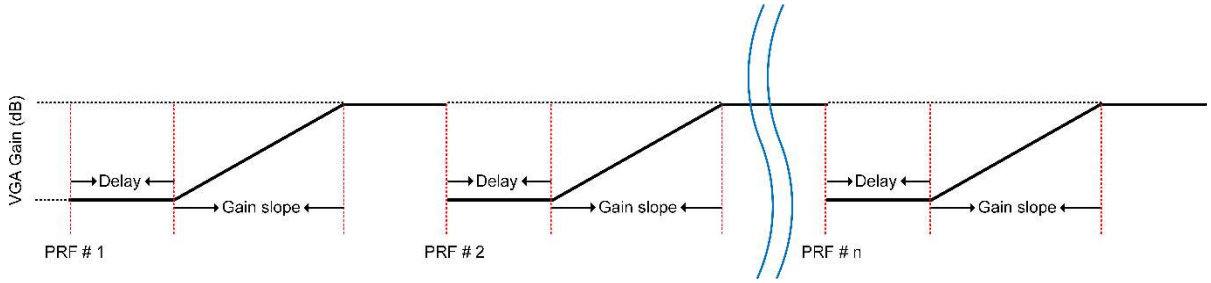

Figure 3.5. VGA adjustment timing according to the depth of the image.

The ADC that operates converting analog RF Data to digital can be changed to various modes depending on the usage environment. the mode of the ADC used in the developed receiving system is changed using the serial interface, and the timing and parameters are shown in Figure 3.6 and Table 3.3.

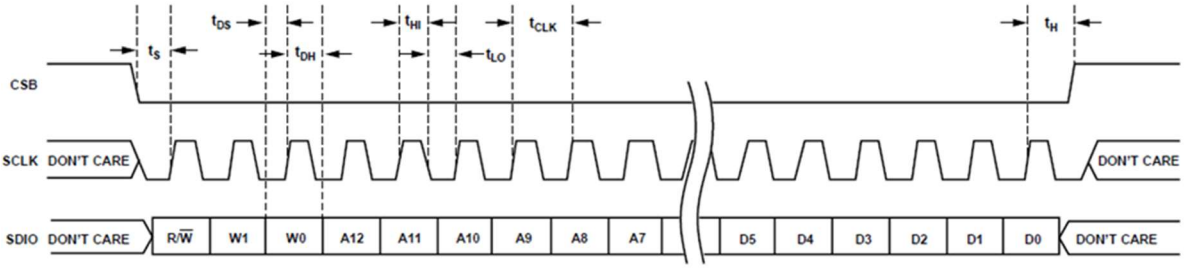

Figure 3.6. ADC serial port interface timing diagram.

Table 3.3. ADC serial port interface timing parameter.

Parameter	Timing (ns)	Description
t_{DS}	5	Setup time between the data and the rising edge of SCLK
t_{DH}	2	Hold time between the data and the rising edge of SCLK
t_{CLK}	40	Period of the clock
t_S	5	Setup time between CSB and SCLK
t_H	2	Hold time between CSB and SCLK
t_{HI}	16	Minimum period that SCLK should be in a logic high state
t_{LO}	16	Minimum period that SCLK should be in a logic low state
t_{EN_SDIO}	1	Minimum time for the SDIO pin to switch from an input to an Relative to the SCLK falling edge
t_{DIS_SDIO}	5	Minimum time for the SDIO pin to switch from an output to an Relative to the SCLK rising edge

Generally, PA and US images have both negative and positive values. therefore, the developed receiving system uses the two's complement data type, which expresses the output mode of the ADC as negative and positive values. The developed receiving system is implemented with a low-spec FPGA, and when receiving ADC data sampled up to 250MHz, timing constraints may occur and the received data may be lost. To overcome this, the output mode of the ADC is set to the Interleave output method, and sample data is received. Interleaved mode

utilizes two 125 MHz clock sources with different phases to receive data at 1/2 clock period of the ADC sampling frequency. Note that the Source clock uses 125 MHz but has a different phase, which allows you to see the effect of 250 MHz sampling. The timing of the Interleaved mode output method is as shown in Figure 3.7, and the detailed parameters for satisfying timing are shown in Table 3.4.

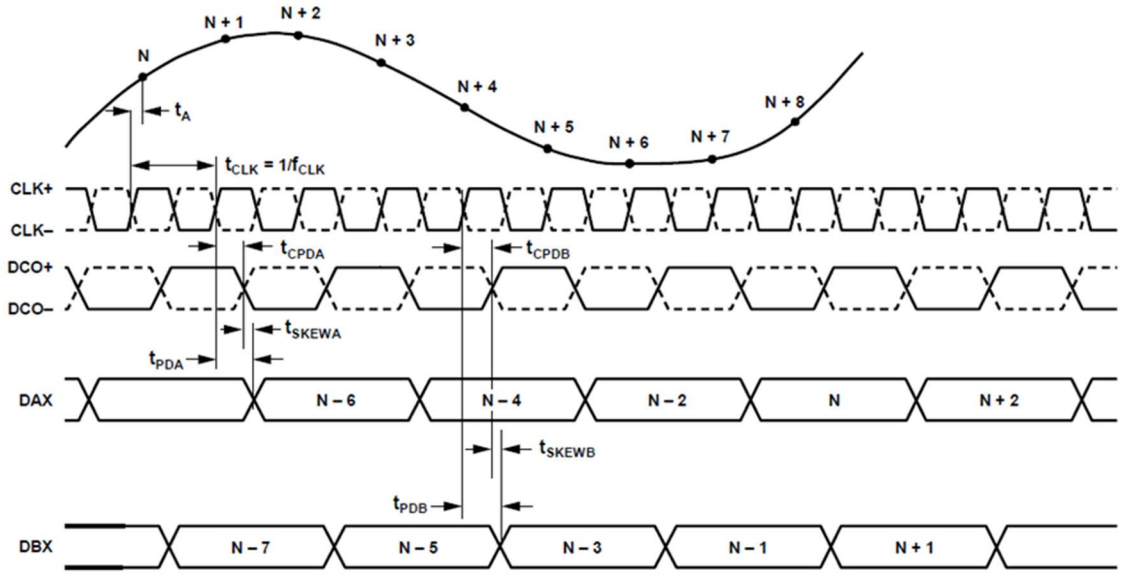

Figure 3.7. ADC interleaved mode data timing diagram.

Table 3.4. ADC interleave mode data switching specification.

Parameter	Min	Typ	Max	Unit
Data Propagation Delay (t_{PDA}, t_{PDB})		3.5		ns
DCO Propagation Delay (t_{CPDA}, t_{CPDB})		3.0		ns
Data to DCO Skew (t_{SKEWA}, t_{SKEWB})		0.5	1.1	ns
Latency		6		Cycles

Also, since the data passed from the ADC is a 125 MHz clock source whose phases are opposite to each other, there is a clock domain crossing (CDC) problem with the internal 100 MHz clock domain. To overcome this, use two dual-port memories, but the writing part of each memory uses a 125 MHz clock source, which is out of phase with each other, as input and uses a valid strobe to perform a write operation, read part uses the internal 100 MHz clock source to double flip-flop the input valid signal and execute the read action with some margin. It is a CDC problem that occurs due to the difference between the input clock and the internal module clock difference, so it is a process that must be processed. The structure and specifications of memory are the same as in Figure 3.8, and the timing for memory access is as shown in Figure 3.9.

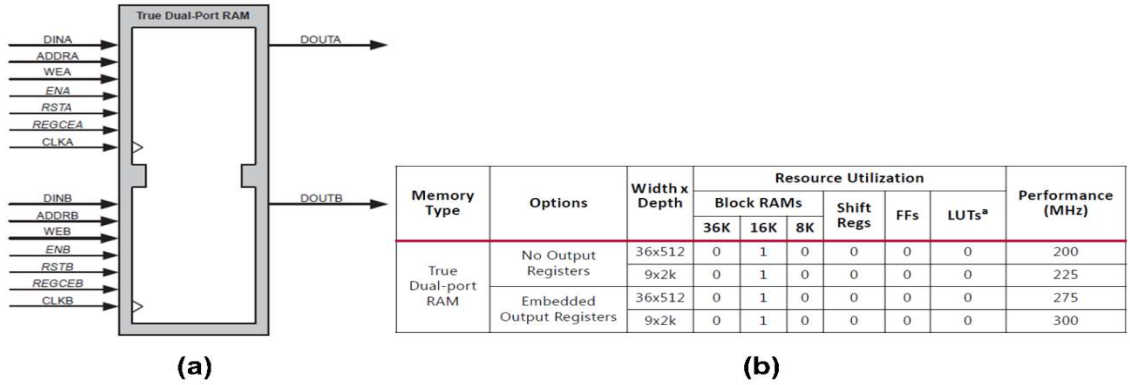

Memory Type	Options	Width x Depth	Resource Utilization						Performance (MHz)
			Block RAMs			Shift Regs	FFs	LUTs[a]	
			36K	16K	8K				
True Dual-port RAM	No Output Registers	36x512	0	1	0	0	0	0	200
		9x2k	0	1	0	0	0	0	225
	Embedded Output Registers	36x512	0	1	0	0	0	0	275
		9x2k	0	1	0	0	0	0	300

Figure 3.8. Structure and specification of true dual port memory.

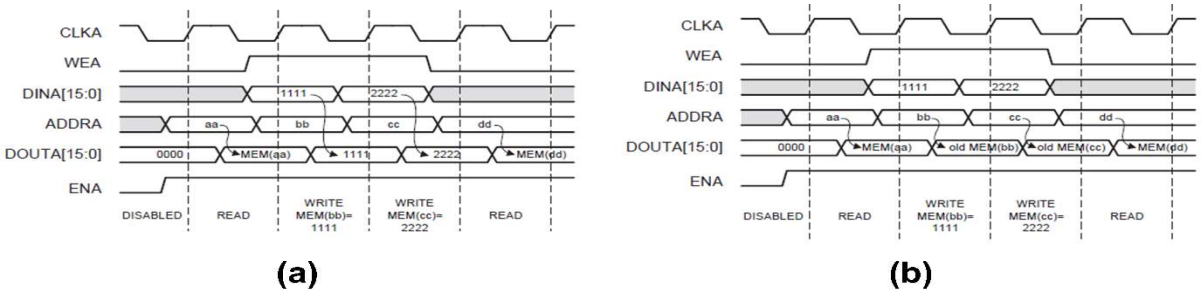

Figure 3.9. Block memory access timing diagram. **(a)** Write first node example. **(b)** Read first mode example.

The host interface that transmits and receives system control signals and transmits the received image data is configured to update the status of the digital front-end module and internal registers through the control path, and the direction of the signal is changed according to control. The Data Path checks the device status through the Control Path control signal and transfers the received images data to the digital back-end module in parallel or performs a Write or Read operation of the data in the internal register. The control signals of the Control Path used at this time are shown in Table 3.5.

Table 3.5. Host interface pin descriptions.

Parameter	Direction	Description
HOST_CS	Input	Select Strobe Flag
HOST_RD	Input	Read Strobe Flag
HOST_WR	Input	Write Strobe Flag
HOST_AD	Input	Register Access for Address
HOST_DQ	In/Output	Register Access for Data
HOST_RDV	Output	Read Valid Strobe Flag
HOST_RF	Output	Received Image Data
HOST_RF_VALID	Output	Received Image Data Valid Strobe Flag
HOST_RF_RUN	Input	Received Data Read Request Strobe Flag
HOST_RF_REQ	Output	Received Data Write Request Strobe Flag
HOST_ENABLE	Input	System Enable Strobe Flag

3.3 Digital back-end module

The FPGA used to implement the Digital front-end module is the Artix-7 XC7A200T Device, a type of Xilinx 7-Series. The 7-Series FPGA logic synthesis tool used VIVADO 2016.2 in an OS Windows 10 (64 bit) environment. In order to transfer the images data received by the Digital front-end module to the Host PC, it plays the role of transmitting the data to 3.2 Gbps (400 MB/s) SuperSpeed using the communication protocol of USB 3.0 Endpoint will be used for data transmission and reception between the Host PC and Device An Endpoint is divided into four according to the data transfer method as shown in Table 3.6, and the Endpoint used to realize system control and image data transfer is shown in Table 3.7, And the architecture and timing for data transfer between the two are shown in Figure 3.10 and Figure 3.11.

Table 3.6. USB protocol transfer type and corresponding transactions.

Endpoint / Transfer Type	Description
Control Transfers	Endpoint that passes device information to the host
Interrupt Transfers	Endpoints that deliver small amounts of data to the host in real time
Isochronous Transfers	Endpoint that delivers continuous data to the host in real time
Bulk Transfers	Endpoints that deliver large amounts of data to the host at a time

Table 3.7. USB 3.0 communication protocol used in implementation.

Endpoint Type	Address	Sync/Async	Description
Wire In	0x00	Asynchronous	Interrupt Transfers
Wire Out	0x20	Asynchronous	Interrupt Transfers
Pipe In	0x80	Synchronous	Bulk Transfers
Pipe out	0xA1	Synchronous	Bulk Transfers

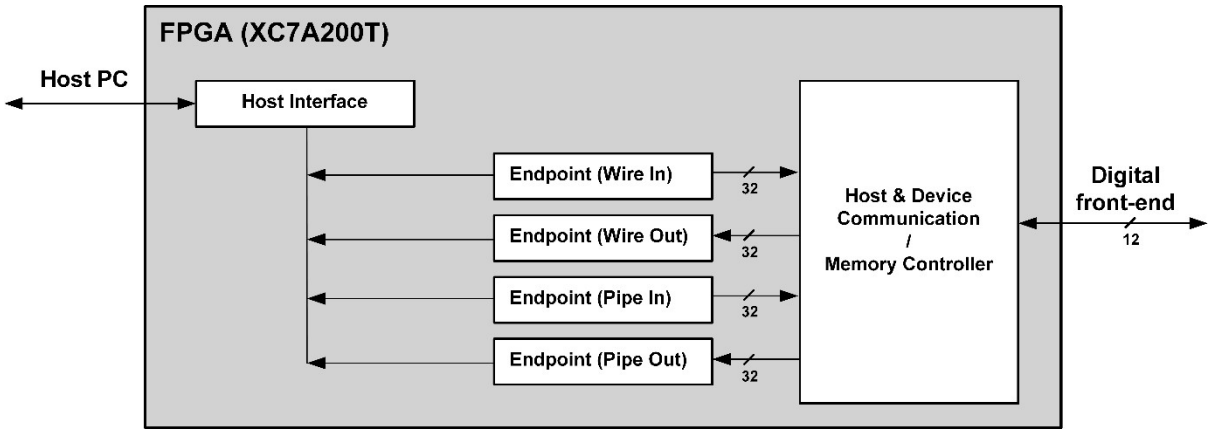

Figure 3.10. Block diagram of the digital back-end block designed and implemented in FPGA.

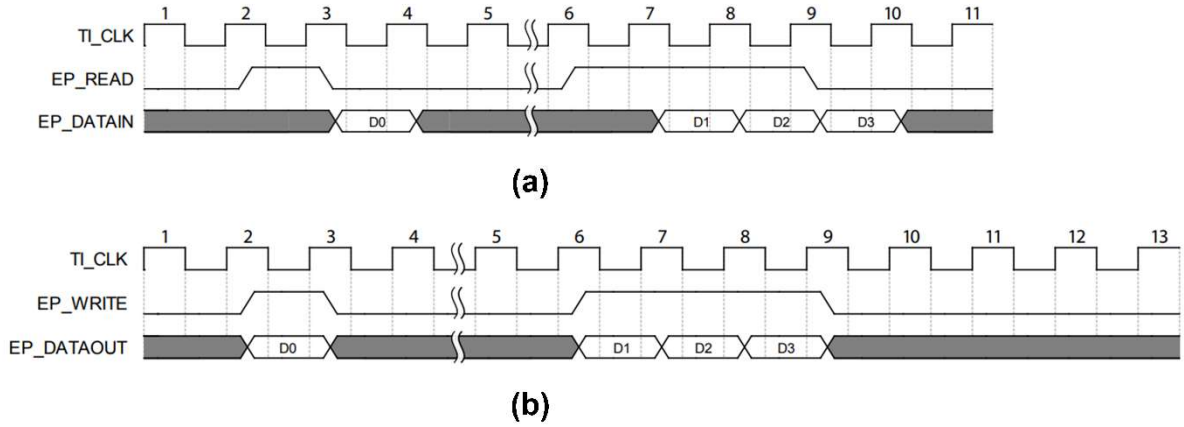

Figure 3.11. Timing diagram for data transmission and reception using USB3.0. **(a)** Timing diagram for data reception. **(b)** Timing diagram for data transmission.

3.4 Application software

The developed and graphical user interface (GUI) was built using the C # programming language that runs on the .NET Framework base for the produced developed reception system and motorized stage controller control, and software development environment and structure are shown in Table 3.8 and Figure 3.12.

Table 3.8. Software development environment.

	Descriptions
OS (Operating System)	Windows 10 (64 bit)
CPU (Processor)	Intel Core i9-10900 CPU 3.7 GHz
RAM (Memory)	Samsung DDR4 16 GBytes X 4
Programming tool	Visual Studio 2019

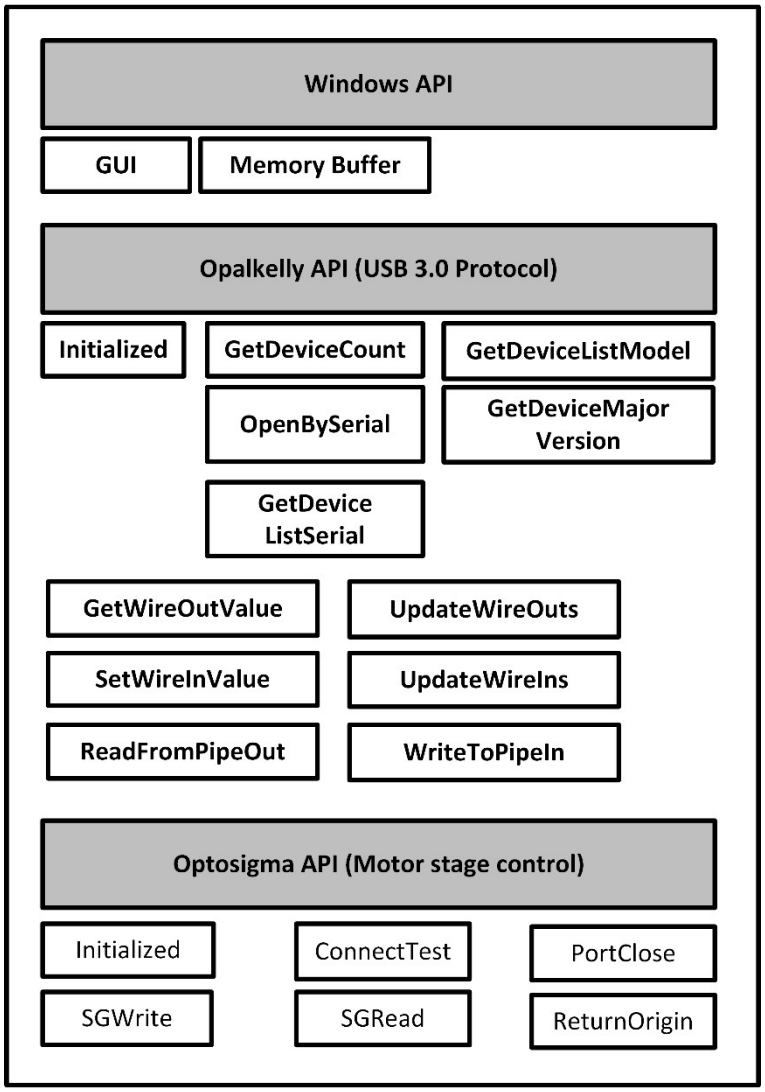

Figure 3.12. Software structure of the developed system.

MotorControl Class defined for motorized stage controller control sets UART as shown in Table 3.9. The host PC and the motorized stage controller are connected through the serial port, and the 3-Axis motor position image data acquisition is controlled using UART Command.

Table 3.9. UART configuration value for motorized stage control.

	UART Configuration Value
Baud Rate	9600
Data Bit	8
Stop bit	1
Parity	None

The Frambuffer Class for controlling the developed reception system and receiving image data will go through an Enumeration process to enable USB communication between the Host PC and Device. At this time,

the Host(PC) will transmit the Device(Digital back-end module) Descriptor information, the Device will be assigned an Address, and the Address will be used to complete the Enumeration after receiving the remaining Descriptor information. The Descriptor, which has the basic information of the USB Device, will receive the Device Configuration information via USB. At this time, the data transmission method and Polling Interval are set according to the type and characteristics of the device via the distributed Configuration information. There are four types of Descriptors as shown in Figure 3.13.

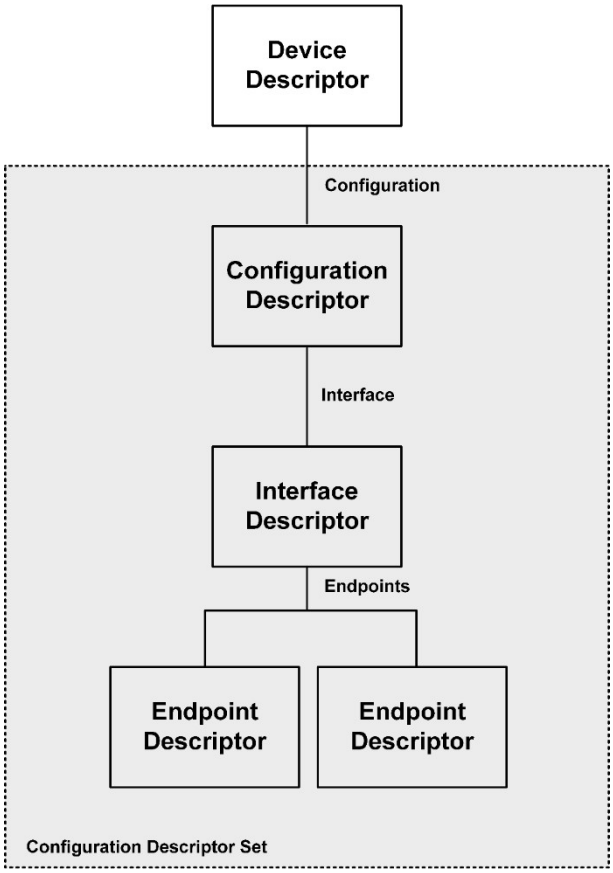

Figure 3.13. Structure of USB device descriptor.

USB Device has a single Device Descriptor and is the most basic information for the device. It has the information of Configuration and Class, Configuration has the information related to the environment setting, and has the power consumption information of Interface. An Interface has information about one function, an Interface of each function is assigned, and the Interface to which the function is assigned can have an Endpoint. An Endpoint is a passage for communication between a host and device and has information such as Endpoint address, data transfer type, and direction. As shown in Table 3.6, there are four types of Endpoints Control, Interrupt, Isochronous, and Bulk. As shown in Table 3.7, the Endpoint used for implementation for data transmission and reception

between the Host PC and Device is composed of four. Wire In and Out Endpoint are methods in which data is transmitted and received in an asynchronous method between the Host and Device. In the case of Wire In a transmission data will be stored using the class method SetWireInValue at the Endpoint that sends data from the Host to the Device. And then, the data saved via the call of UpdateWireIns will be sent from the Host to the Device. In the case of reception, the data from the Device is received via GetWireOutValue and stored in the internal data structure. Then, the data will be received by the Host via the call to UpdateWireOuts. For Pipe In and Out Endpoint, the Host becomes the master, and the device is salved so that multiple transactions can be sent and received in an synchronous method. In the case of Pipe In, data is sent from the host to device by Bulk Transfer. Data is sent using Class Method WriteToPipeIn at Endpoint. The Host will transfer data to 8 bit words through Endpoint but will have a 32 bit word band on the Device. In the case of Pipe Out, it is a method to receive the data from Device to Host by Bulk Transfer by Host request. Also, the Device sends data to 8 bit word, but the Host transfers data to 8 bit word.

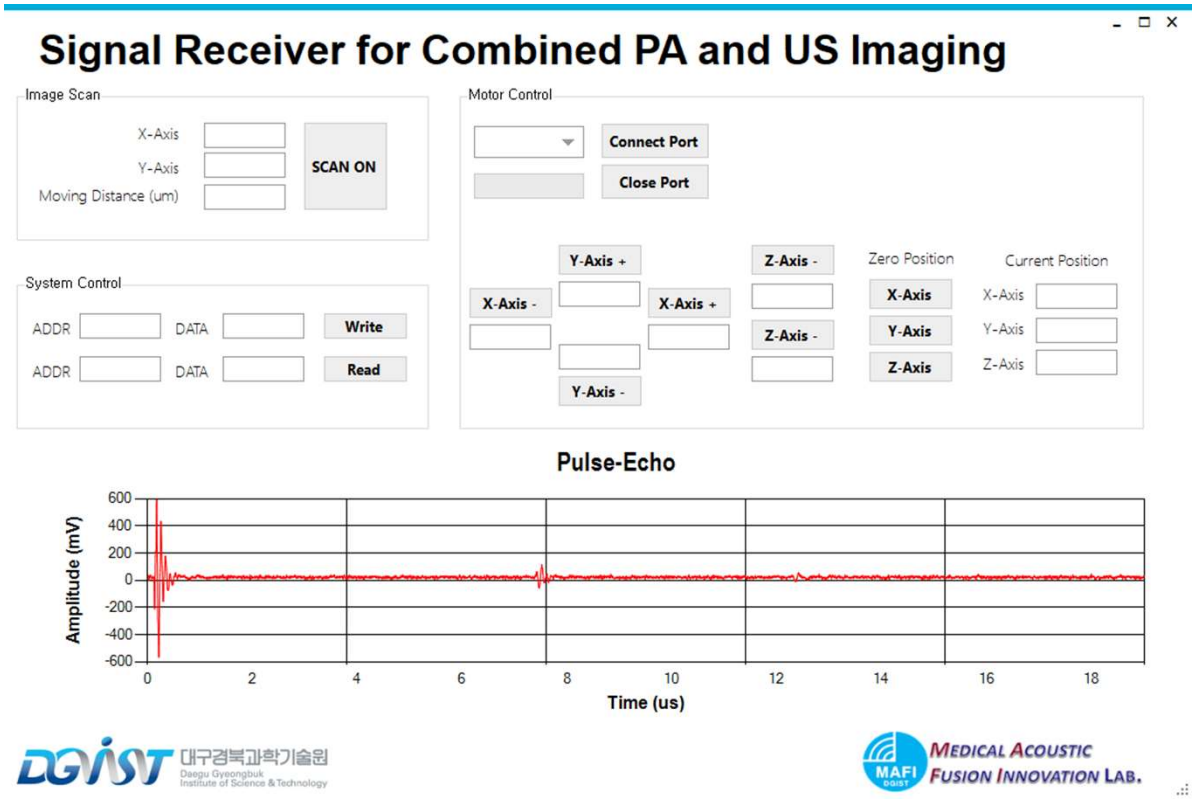

Figure 3.14. Graphic user interface of the combined PA and US system.

IV. EXPERIMENTS FOR DEVELOPED RECEIVE SYSTEM PERFORMANCE EVALUATION

4.1 Analog front-end performance evaluation

The key function of the developed signal receiving module is to amplify the signal in the desired frequency range with high gain flatness. First, the transfer functions of the HPF and LPF were measured using a network analyzer (E5061B, Keysight Technologies, Santa Clara, CA, USA). For the measurement, a power of 0 dBm was applied to the input port of each filter. As shown in Figures 4.1(a) and (b), it was verified that the implemented filters had the designed cutoff frequencies: 5 MHz for the HPF and 70 MHz for the LPF. The amplification performance of the developed module was evaluated by applying a power of –40 dBm to the input of the protection block and measuring the transfer function at the output of the second VGA (see Figure 2.1). When the gains of each VGA were set to be –6 dB (i.e., a total of –12 dB), the total amplification gain was measured to be about 24 dB within the desired operating frequency range (i.e., 5 – 70 MHz). The theoretical gain of 28 dB was reduced by 4 dB due to the signal attenuation: 3 dB in the protection block and 1 dB in the two analog filters (see Figure 4.1(c)). The maximum amplification gain was measured to be about 72 dB when the two VGA gains were set to be the maximum (i.e., 18 dB each). In each amplification gain, the flatness over the operating frequency range was measured to be less ± 1 dB. As a result, it was confirmed that the amplification performance of the developed signal receiving module met the design specifications.

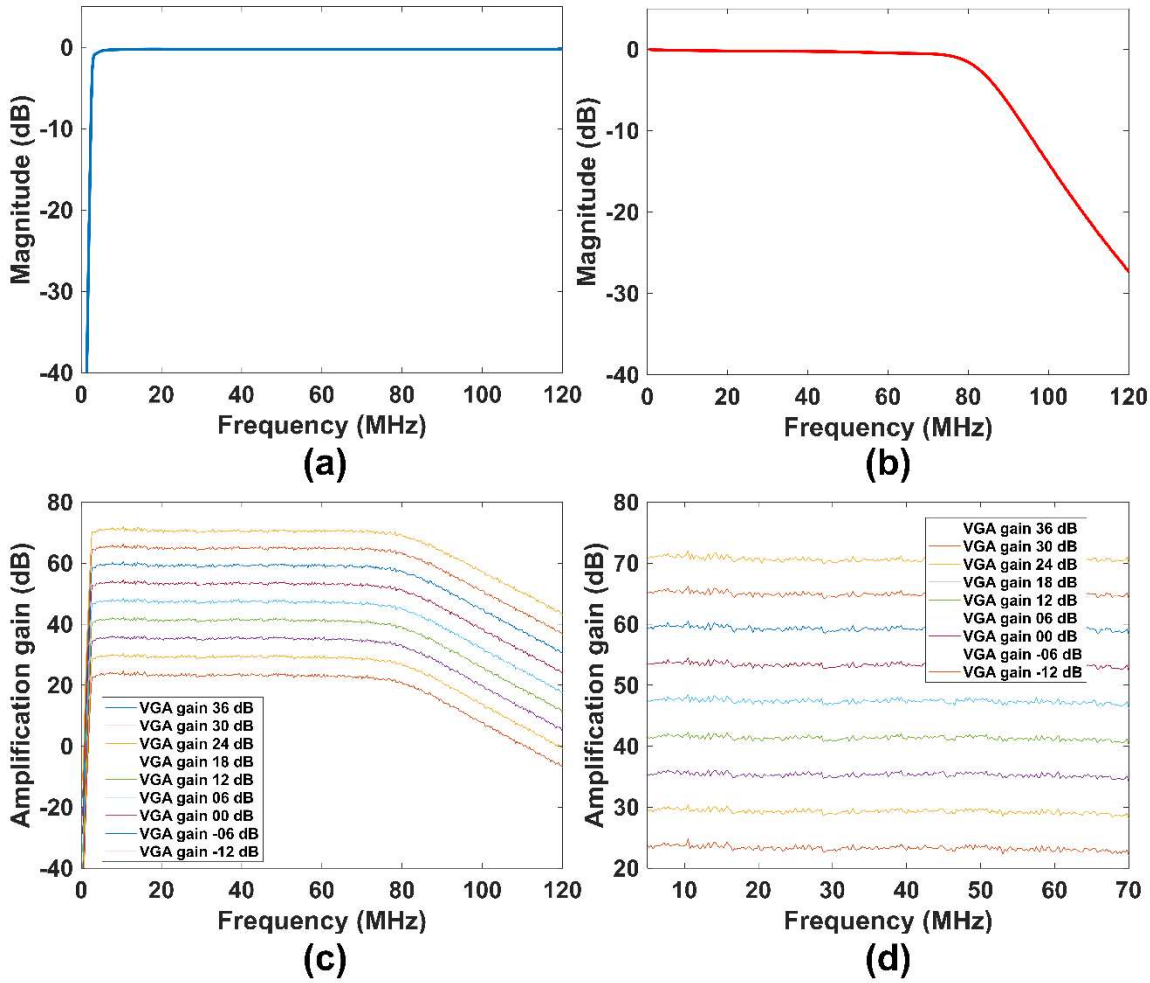

Figure 4.1. Measured transfer functions of **(a)** the analog HPF and **(b)** LPF, **(c)** the measured amplification gains of the developed signal receiving module when the total gain of the two VGAs was changed from –12 dB to 36 dB, and **(d)** the zoom-in version of the amplification gains over the operation frequency range, i.e.., 5 – 70 MHz.

4.2 Laser beam FWHM (full width at half maximum) measurement

To validate the performances of the laser beam distribution, the integration with transducer and optical modules (i.e., objective lens and optical fiber) was implemented. The transducer and optical module integrated assembly was designed by Inventor (Autodesk, Inc., San Rafael, CA, USA), and the transducer and optical module were coaxially aligned, as shown in Figure 4.3.

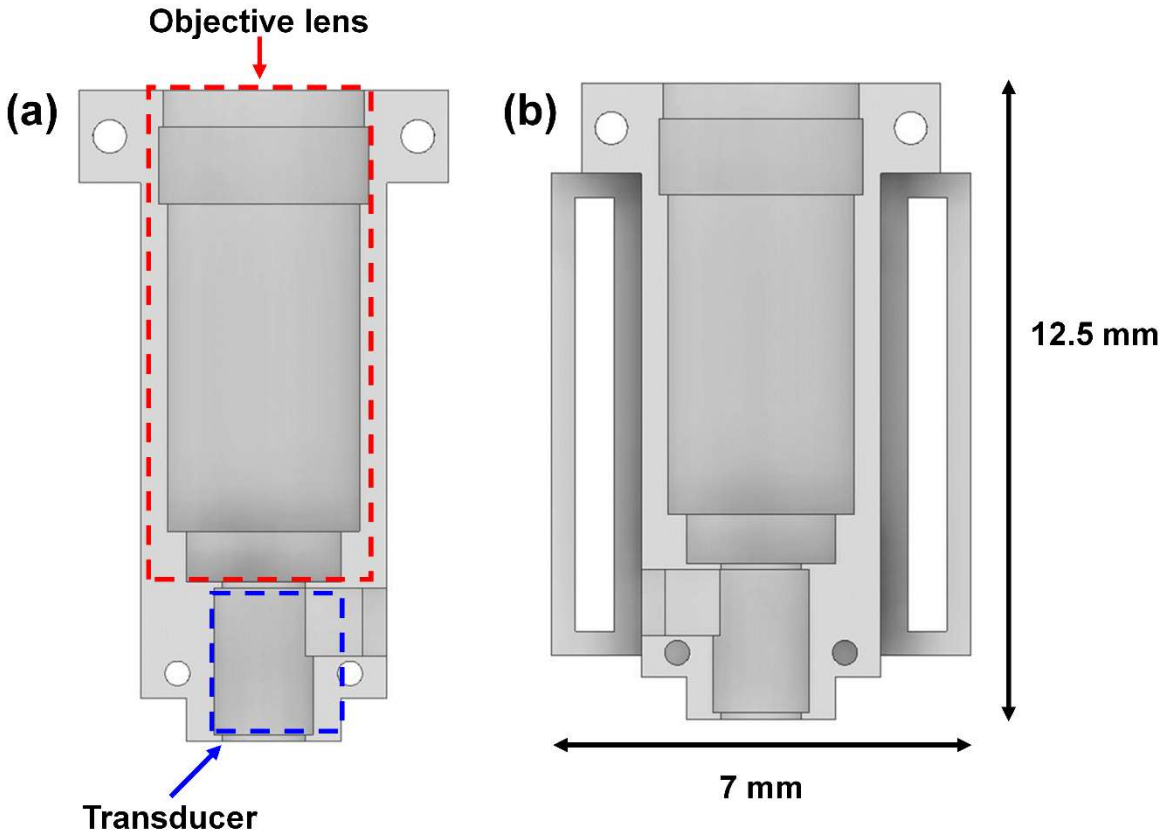

Figure 4.2. Cross-sectional illustration of the prototype-designed housing. **(a)** Bottom side of the housing and **(b)** Top side of the housing.

The Assembly is shown in Figure 4.2. has a groove for mounting the objective lens and a groove for mounting the transducer. The prototype of the assembly is manufactured using a 3D Printer (3DWOX2X, Sindoh, Co., Ltd., Seoul, Korea), and the material used for 3D Printing is Polylactic acid (3DP200PRE-RQ, Sindoh, Co., Ltd., Seoul, Korea). Figure 4.3. shows how the coaxial arrangement of the objective lens and the transducer was achieved by using the prototype assembly that was manufactured.

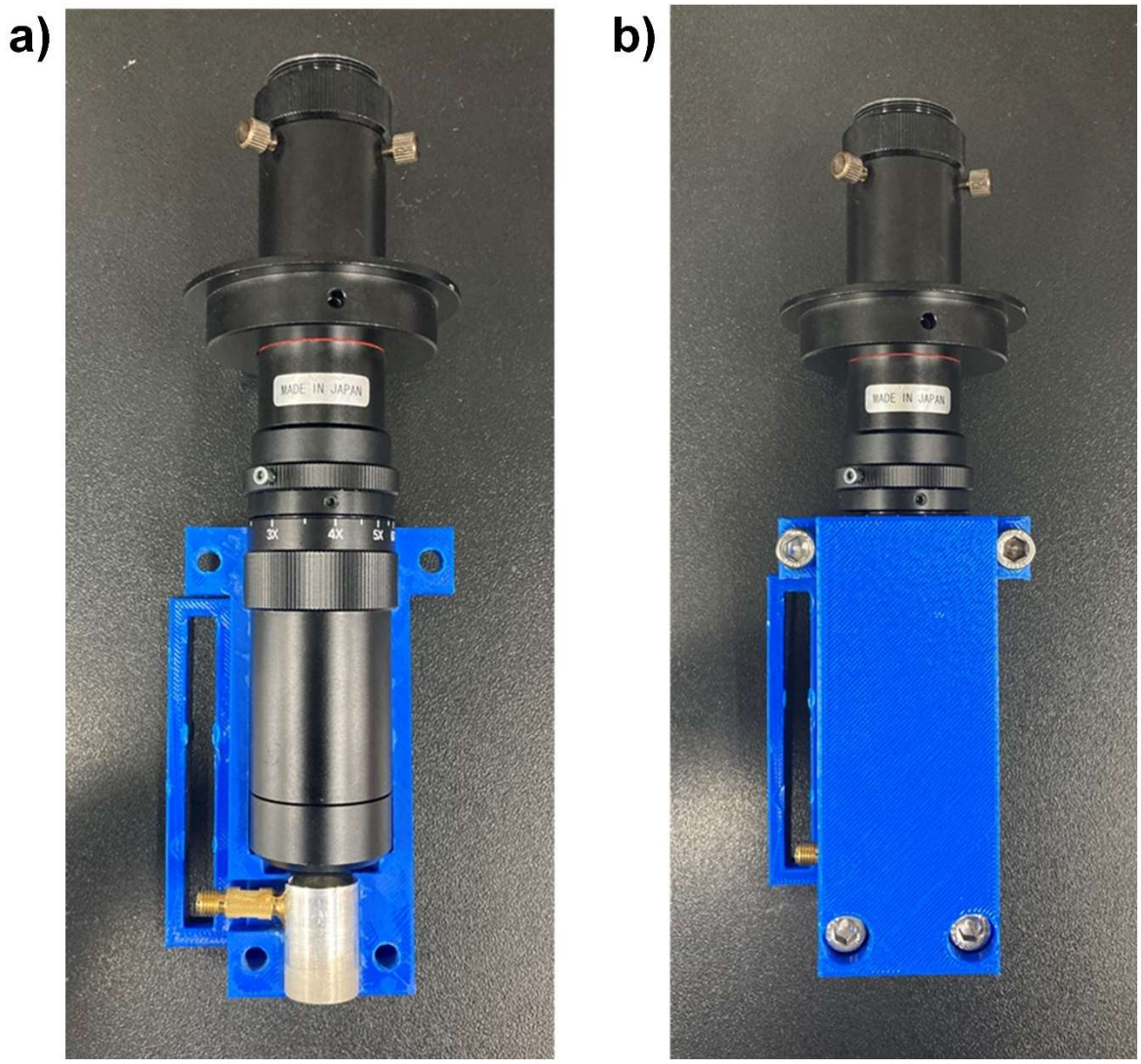

Figure 4.3. Photograph of the objective lens and transducers mounted on the assembly.

To measure the light energy distribution passing through the transducer An Nd:YAG laser excitation system (Surelite III-10 and Surelite OPO Plus, Continuum Inc., Santa Clara, CA, USA) was used to deliver the laser through the optical fiber bundle and objective lens. The laser beam profile measurements were taken at the working distance (i.e., without lens) of the transducer using a Charge-coupled Device (CCD) camera (CoolSNAP MYO, Photometrics, Tucson, AZ, USA) and a mono telephoto macro lens as shown in Figure 4.4. And then, the measured energy was normalized by the reference value to eliminate the wavelength-dependent fluctuation of light energy generated from the Nd:YAG laser system [9]. As a result, laser beam resolution was measured at FWHM (full width at half maximum) 2.95 mm as shown in Figure 4.5.

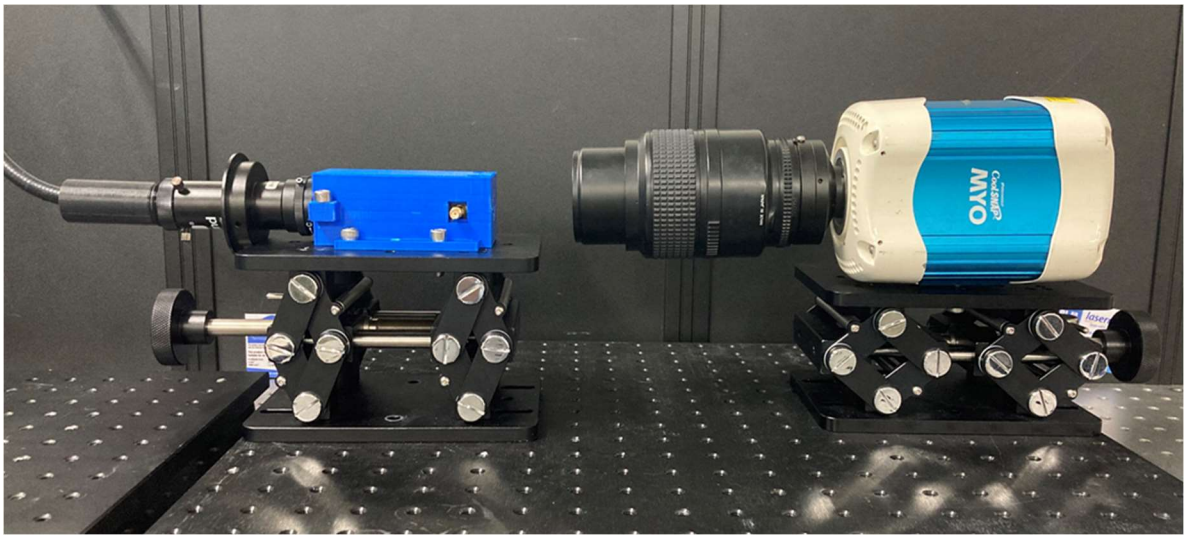

Figure 4.4. Photograph of the measurement of the distribution of a laser passing through a transparent transducer.

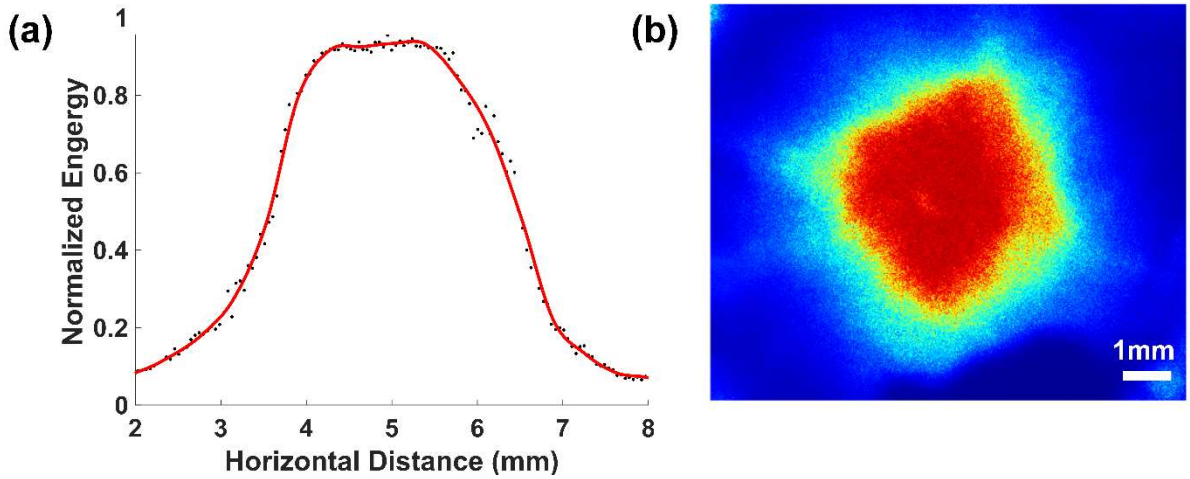

Figure 4.5. light distributions measured at the focal point of the transducer (i.e., 6 mm). **(a)** the distributions along the horizontal axis (dots) and the corresponding smoothing spline fitting curve (red line), **(b)** measured after the irradiated light penetrated.

4.3 Selection of Optimal Laser Wavelength

To select the optimal laser wavelength for the PAM image, a leaf skeleton acrylamide[15,16] phantom with a height of 10 mm and a width of 110 mm was fabricated as shown in Figure 4.6. The leaf skeleton is dyed with blue oil-based ink (H8940-01LC, Inktech Co., Ltd., Gyeonggi-do) to increase the absorption coefficient of laser energy and increase the intensity of the PA signal. Then, use various sizes of liquid and liquid water (Sigma-Aldrich, Inc., MO) as shown in Table 4.1 to fabrication acrylamide phantom.

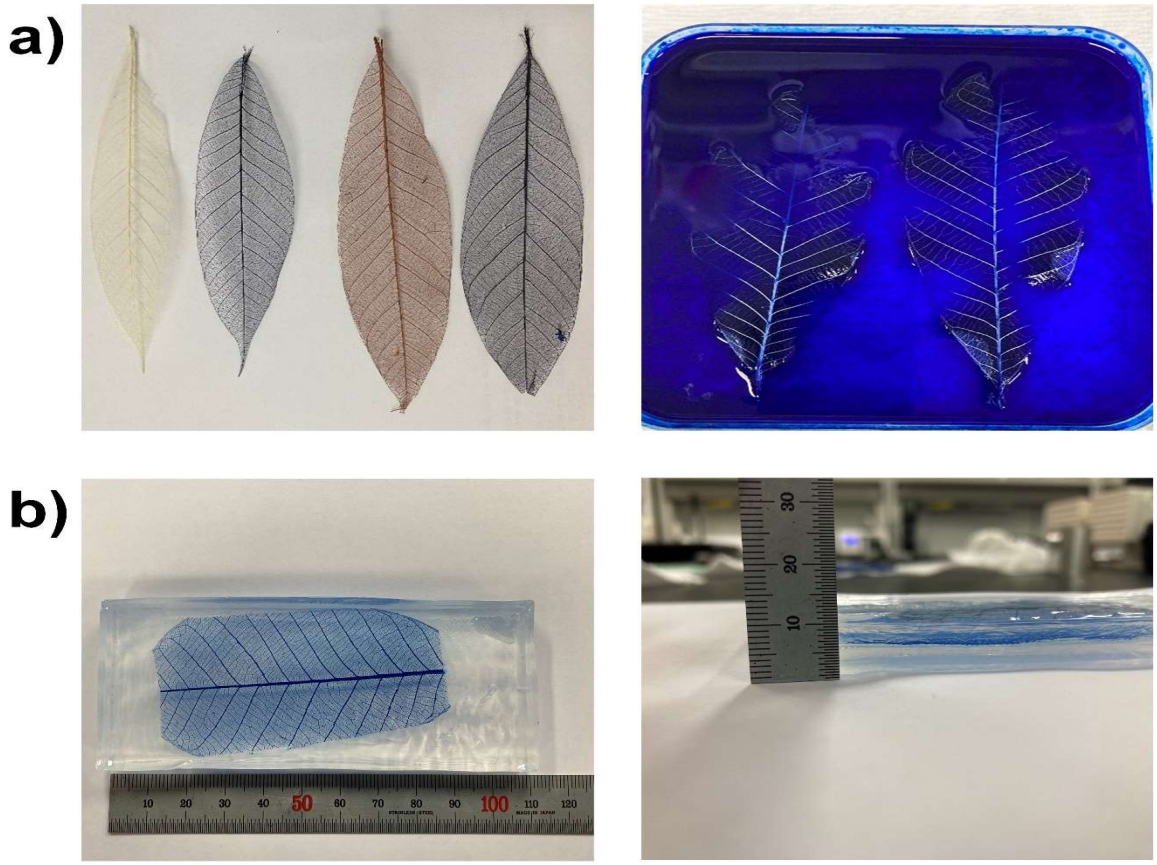

Figure 4.6. Photograph of the fabrication of leaf skeleton vessel phantom. **(a)** Blue ink dyeing process to increase PA signal intensity and **(b)** Custom-made acrylamide phantom consisting of height 10 mm and width 110 mm.

Table 4.1. Materials used to fabrication the acrylamide phantom.

Component	Description
Acrylamide/Bis-Acrylamide 40%	BioReagent, suitable for electrophoresis, 19:1
Tetramethyl-ethylenediamine	BioReagent, suitable for electrophoresis, ~ 99%
Trizma® base, Sigma-Aldrich	Primary Standard and Buffer, ≥ 99.9% (titration), crystalline
Ammonium persulfate	for molecular biology, suitable for electrophoresis, ≥ 98%
Trizma® hydrochloride	reagent grade, ≥ 99.0% (titration), crystalline

The intensity of the PA signal was measured using the fabricated phantom. The intensity of the PA signal was measured while changing the 532 nm single wavelength laser and the laser wavelength in the range of 680 nm to 960 nm at 10 nm intervals. Note that the change in PA signal intensity is linearly proportional to the optical absorbance of the subject. The phantom fabricated as shown in Figure 4.7 absorbed the laser to the maximum when the wavelength was 532 nm. The laser wavelength of 532 nm was considered the optimum wavelength for PAM imaging.

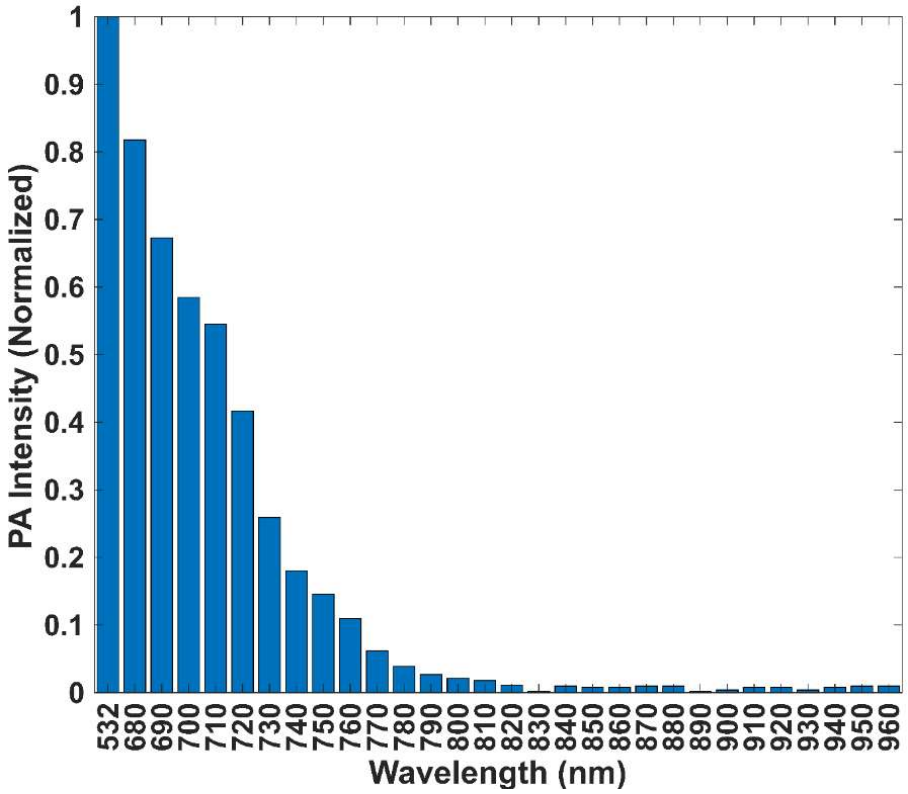

Figure 4.7. The plot of changes in photoacoustic signal intensity as a function of laser wavelength for leaf skeleton vessel phantom.

4.4 Performance evaluation of the B-mode using PA and US imaging

The effect of the two VGAs on SNR performance was ascertained based on the B-mode PA image of wires with a diameter of 100 um and the performance with the commercial receiver system was compared and evaluated. For PA image acquisition, A four gold wire with a diameter of 100 um was placed at a position of 5.8, 6.6, 7.7, 8.2 mm in the Axial direction to acquire PA imaging. In other words, the first wire was at the focus of the transducer, and the third and fourth wires were located outside the DOF (depth of focus). For PA imaging, 601 scanlines were acquired at 20 um intervals. commercially receive system cannot adjust the amplification according to the depth of imaging, so acquired an image of PA with a fixed amplification 32 dB gain. On the other hand, the amplification gain of the developed system increased linearly at 32 dB at a depth of 5.8 mm and at 36 dB at a depth of 7.8 mm to acquire PA images. The SNR of each receiving system was calculated using equation (1) [17]. At this time, $mean_i(\cdot)$ is the average function of a variable i. For this study, L was set to be 4. Note that Equation (1) provides the SNR plot as a function of imaging depth.

$$SNR(j) = mean_i\left(20\log_{10}\left(\sqrt{\frac{\sum_{n=-L/2}^{n=L/2} E_S\,(i,j-n)^2}{\sum_{n=-L/2}^{n=L/2} E_N\,(i,j-n)^2}}\right)\right), \quad (1)$$

The B-mode PA images acquired by the commercial and the developed systems are shown in Figures 4.8(a) and (b), respectively. Near the focal depth, the two wire images labeled by A and B were clearly visible in both systems, but the SNRs of the developed system were 5.3 dB and 6.7 dB higher than those of the commercial system: 20.0 dB vs. 14.7 dB for the label A image and 18.3 dB vs. 11.6 for the label B image (see Figures 4.8(c) and (d)). Since the third and fourth wires (label C and D) were located outside the DOF, the PA images acquired by the commercial system were barely seen, but those by the developed system were more clearly observed due to the depth-dependent variable gain. The SNRs of the developed system were 11.6 dB for the third wire image and 10.3 dB for the fourth wire image, whereas those were 6.6 dB and 6.4 dB, respectively (see Figures 4.8(e) and(f)).

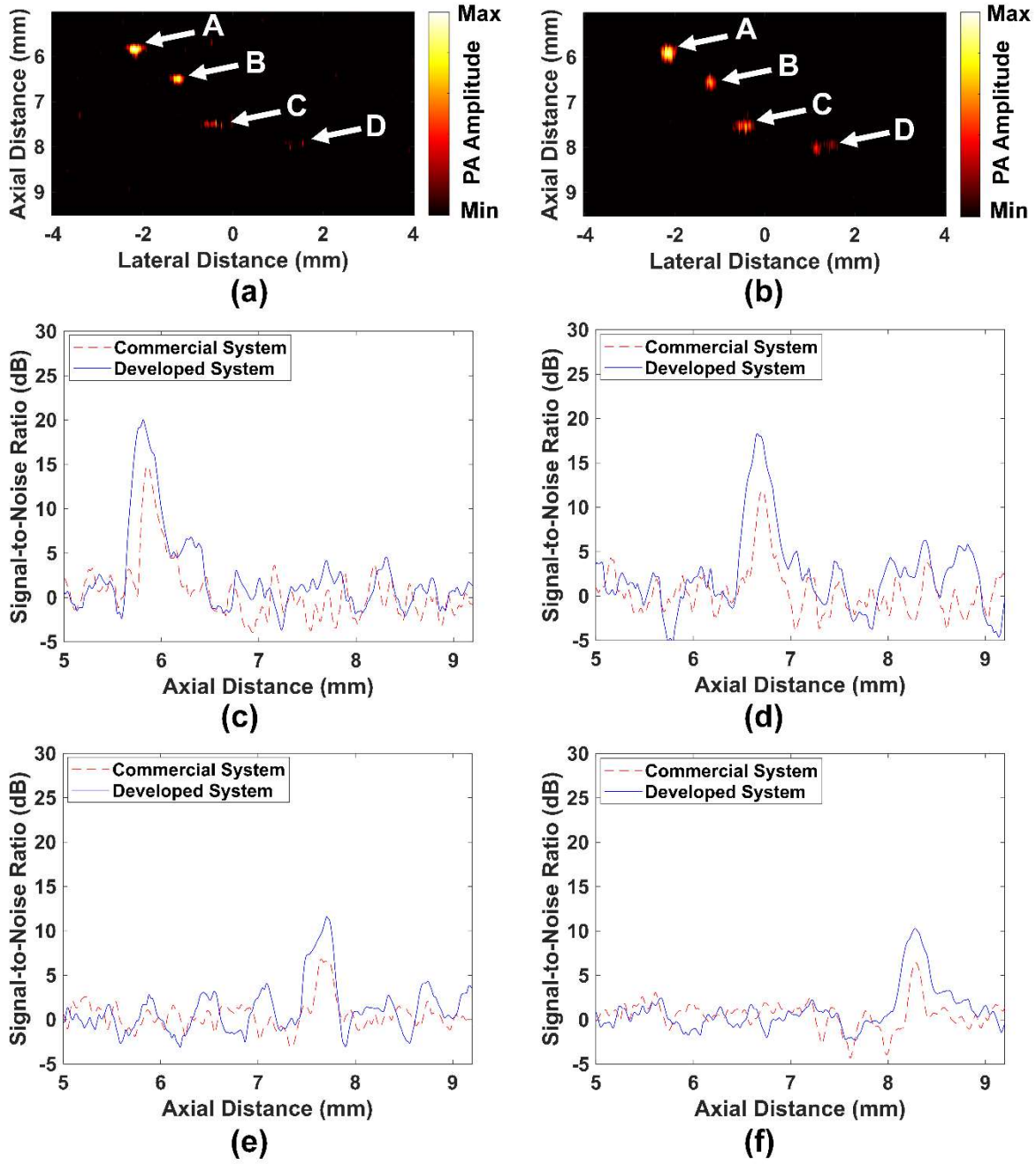

Figure 4.8. VGA performance evaluation using B-mode PA Image. **(a)** Image acquired by the development receive system. **(b)** Image acquired by the developed receive system. SNR plots as a function of imaging depth for the targets labelled by **(c)** A, **(d)** B, **(e)** C, **(f)** D in **(a)** and **(b).**

Furthermore, the effect of the two VGAs on CNR performance was ascertained based on the B-mode US images. To acquire B-mode US images, a tissue-mimicking agar phantom was fabricated[15,16] and four cysts with a diameter of 1.5 mm were placed at positions 3, 5, 10, and 11 mm in the axial direction to acquire US imaging.

Table 4.2. Materials used to fabrication the tissue-mimicking agar phantom

Component	Description
Agar	For molecular biology
Scatter	Glass spheres, 9 ~ 13 um particle size

In other words, the second cyst was at the focus of the transducer, and the other cyst was located outside the DOF. For imaging, 1251 scanlines were acquired at 20 um intervals. commercially receive system cannot adjust the degree of amplification according to the depth of imaging, so acquired an image of US with a fixed amplification 32 dB gain. On the other hand, the amplification gain of the developed system increased linearly at 32 dB at a depth of 3 mm and at 48 dB at a depth of 11 mm to acquire US images. And then CNR performance evaluation was performed for quantitative analysis. After extracting the signals from the solid square and dotted square depth regions of Figure 4.9 calculate using Equation (2) [18].

$$CNR = \frac{|\mu_T - \mu_B|}{\sqrt{\sigma_{T^2} + \sigma_{B^2}}} \tag{2}$$

At this time μ_T is the average value of the Envelop signal measured in the solid square area and μ_B is the average value of the Envelop signal measured in the dotted square area. σ_T and σ_B are standard deviation values from the signal in each region. The receiving system developed as seen in Figures 4.9 shows the ability to distinguish cysts after the transparent transducer focusing point used in the experiment. On the other hand, in the commercial receiving system, the position cyst after the focusing point is not surely classified due to the intense spectacle noise of the image. And the CNR performance evaluation was performed as shown in Table 4.3.

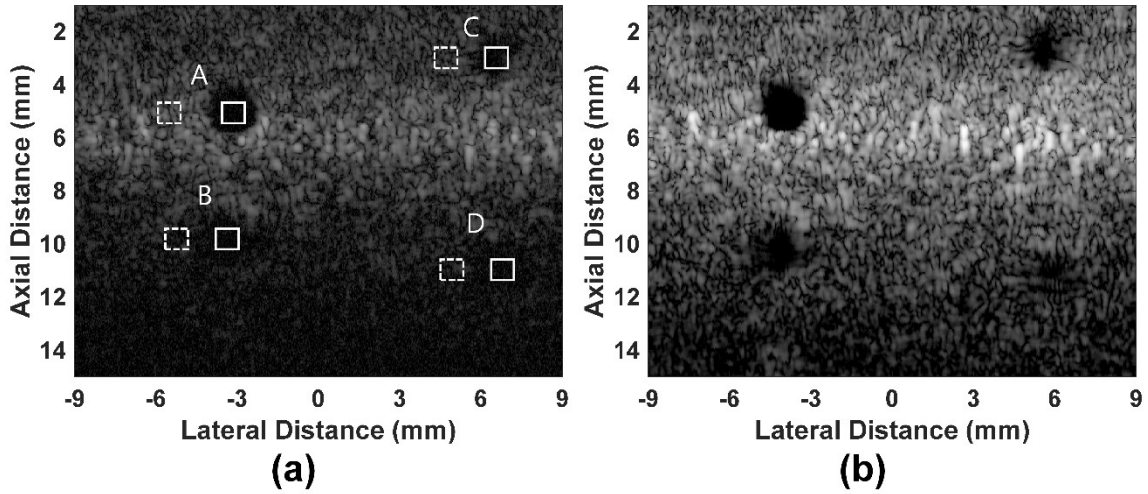

Figure 4.9. VGA performance evaluation using B-mode US Image. **(a)** Image acquired by the commercial receive system. **(b)** Image acquired by the developed receive system. CNR was measured using the envelope signals within the two white boxes.

Table 4.3. Comparison of the performance of CNR between commercial system and developed system.

Receive System	Cyst Location			
	A (5 mm)	B (10 mm)	C (3 mm)	D (11 mm)
Commercial	1.5785	0.8249	1.3469	0.5944
Developed	1.8142	1.4004	1.6661	0.7912

4.5 Performance evaluation of the PAM Imaging

The characteristics of the Optically Transparent Transducer used for PAM image performance evaluation are show those in Table 4.4.

Table 4.4. Characteristics of the custom-made optically transparent focused transducers.

Center frequency (MHz)	11.2
-6 dB fractional bandwidth (%)	23 (i.e., 9.9 to 12.5 MHz)
Element size (mm)	7 x 7
Focused focal length (mm)	6
Depth of focus (mm)	1.78
Lateral resolution (um)	182

A Leaf skeleton vessel phantom was fabricated to compare the performance of the developed receiver system and the commercial receiver system and AR-PAM images were acquired. As shown in Figure 4.11 the phantom was placed inside the water tank of the motorized 3-axis XYZ stage (SGSP26-100, SIGMAKOKI Co. Ltd., Tokyo, Japan) and excited using the laser optical fiber bundle and the objective lens (VZM™ 600i Zoom Imaging Lens, Edmund Optics Inc., Barrington, USA) using the Nd: YAG laser system (Surelite EX and Surelite OPO Plus, Continuum Inc., Santa Clara, CA, USA). At this time the Laser used was Pulse 7 ns, pulse repetition frequency 10 Hz, wavelength 532 nm, and Energy was 1.1 mJ/cm^2 [19]. An experimental environment as shown in Figure 4.11 was constructed and the AR-PAM images signal of the leaf skeleton vessel phantom was acquired using the developed receive system. Then to quantitatively evaluate the performance of the developed receive system an additional AR-PAM images signal was acquired using a commercial receive system (UT340, UTEX Scientific Instruments Inc., Mississauga, ON, Canada) and a gage card (CS1422, Gage Applied Technologies Inc., Montreal, QC, Canada) in the same environment [18].

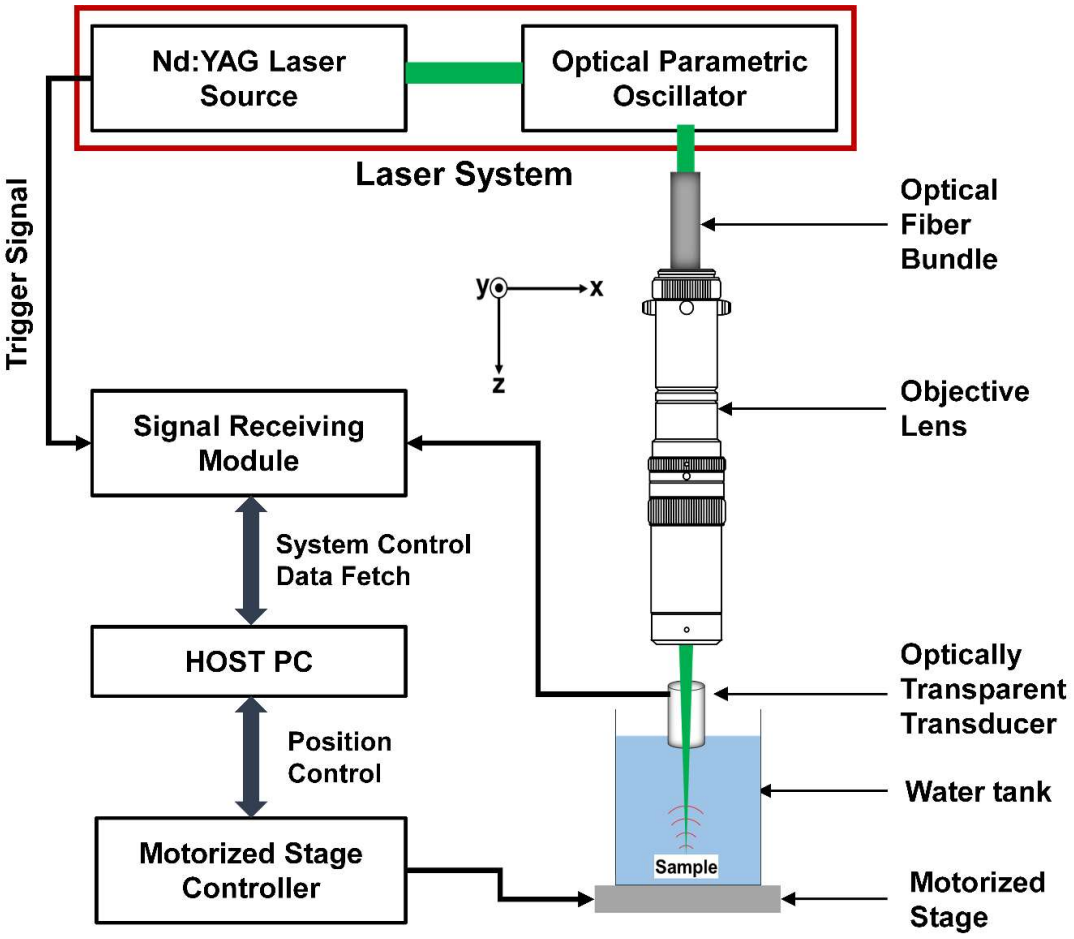

Figure 4.11. Block diagram of the developed imaging system for PAM

The scan area of the image was set to the area of interest of 10mm x 6mm. The scanning interval was 20 um and 150,801 scan line data was acquired. For the AR-PAM imaging, the VGA gain was fixed to be –6 dB, so that the total amplification gain of the developed system was 32 dB. The gain of the commercial signal receiving system was also set to be 32 dB. The leaf skeleton vessel phantom used for image acquisition has a thickness of 100 um, and the DOF of the transducer used for image acquisition is 1.78 mm, which complements frequency-dependent attenuation. Therefore, there was no need to change the VGA gain to compensate for the frequency-dependent attenuation.

Image performance was evaluated quantitatively by comparing the CNR and SNR performances. For CNR performance comparison using the signals in the white solid line square and dotted line rectangular areas in Figure 4.12b,c. Calculated using equation (3) [20].

$$CNR = \frac{|\mu_T - \mu_B|}{\sqrt{\sigma_{T^2} + \sigma_{B^2}}} \tag{3}$$

As shown in Figure 4.12 the CNR measured using the developed receive system was 36 dB and the CNR measured using a commercial receive was 33 dB. Developed receive system demonstrated superior CNR performance of at least 3 dB compared to commercial receive system. SNR was obtained as a function of scanlines consisting of one line on a PAM image by using equation (4).

$$SNR(i) = 20\log_{10}\left(\frac{\max_j\{E_S(i,j)\} - \sigma_j\{E_N(i,j)\}}{\sigma_j\{E_N(i,j)\}}\right), \tag{4}$$

At this time where i and j indicate the scanline and the sample, $E_S(i,j)$ and $E_N(i,j)$ is the j^{th} signal and noise envelope samples of the i^{th} scanline, respectively, and $max_j(\cdot)$ and $\sigma_j(\cdot)$ are functions representing the maximum and the standard deviations of the samples indicated by j on a scanline i. As shown in Figure 4.12 the SNR values corresponding to the line indicated by the white dashed line in Figure 4.12(b), which were calculated using Equation (4). The average SNRs of the developed and the commercial systems were 35.7 dB and 31.0 dB, respectively; in terms of SNR, the developed system outperformed the commercial system by 4.7 dB.

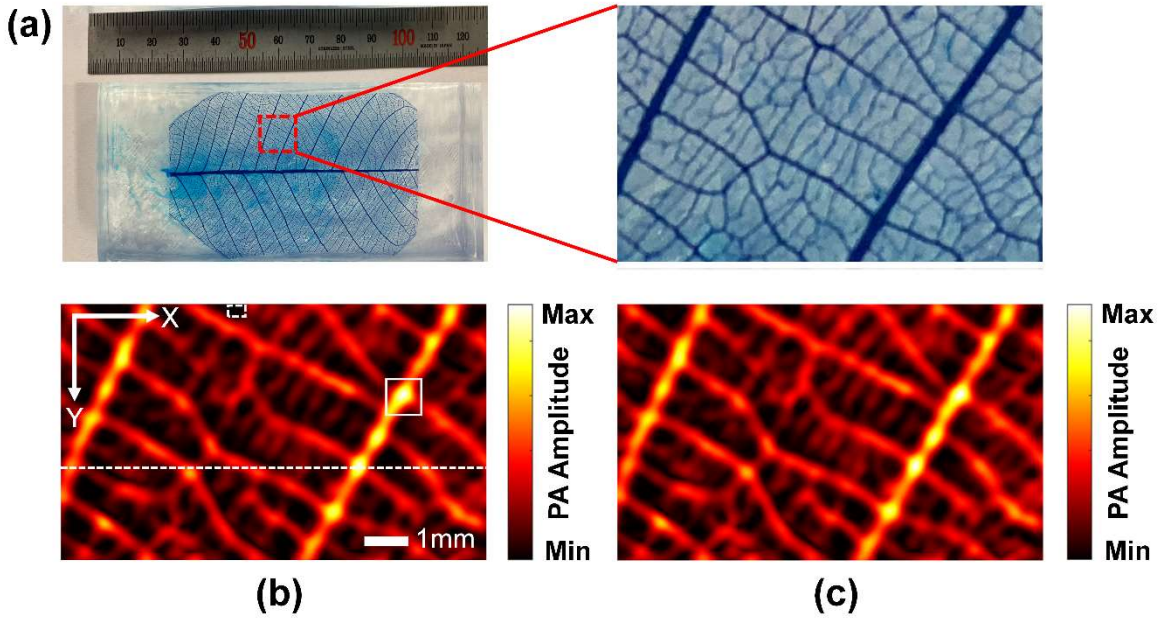

Figure 4.12. (a) Photographs of the stained skeleton leaf vessel phantom (left) and the zoom-in version of the imaging area (right), **(b)** PAM image acquired by the combination of several pieces of commercially available equipment, and **(c)** PAM image by the developed system. SNR was measured using the PA signals generated in the region indicated by the white dashed line in **(b)**, and CNR was measured using the envelope signals within the two white boxes in **(b)**.

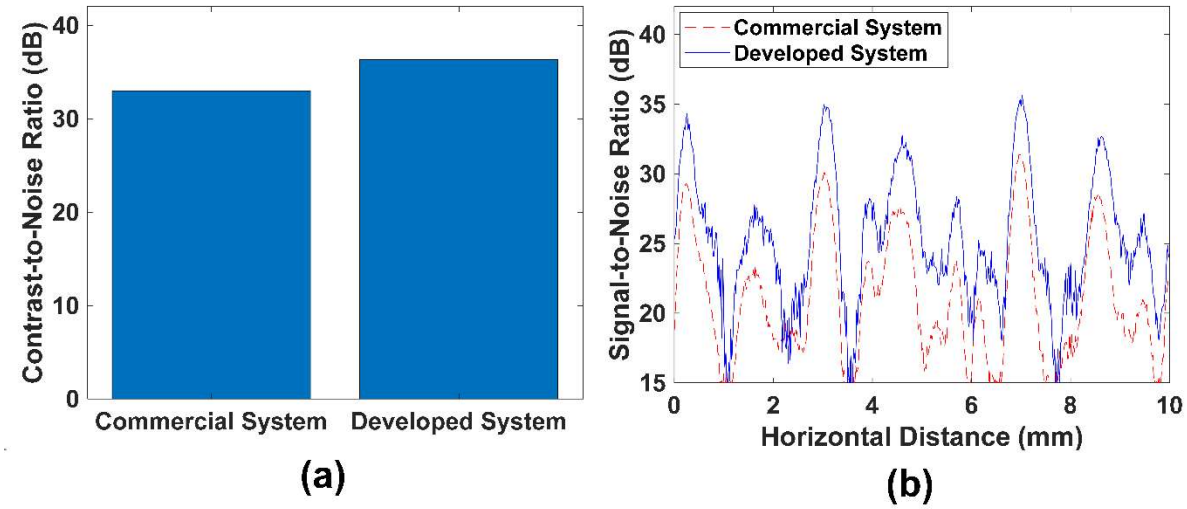

Figure 4.13. PAM image performance evaluation. **(a)** Contrast-to-Noise Ratio (CNR) acquired from Figure 4.12 b, c. **(b)** Signal-to-Noise Ratio (SNR) acquired from Figure 4.12 b, c.

IV. DISCUSSION & CONCLUSION

In the thesis, I have proposed a low-noise reception system that can combine photoacoustic and US images. the developed system is capable of improving both SNR and CNR of B-mode and PAM images, compared to the commercial system. The excellent performance of the developed system stems from the unique arrangement of two LNAs and two VGAs. In particular, it has been seen that the ATGC function based on the two VGAs is beneficial for B-mode and AR-PAM of which imaging depth is deeper than that of OR-PAM. A useful feature of the developed system is that the operation bandwidth can be easily changed by adjusting the cutoff frequencies of both analog HPF and LPF. The operation frequency can be increased up to 120 MHz.

As a future task, studies and experiments on image performance evaluation using a high-frequency transducer, PA and US combined image, which was not evaluated in this thesis remains. Although the high-frequency transducer has a low sensitivity of the received signal and has limitations on image depth, the high operating frequency and wide frequency bandwidth of the developed system are expected to enable high-resolution image acquisition compared to commercial systems. In addition, the Nd:YAG laser, which is commonly used in optoacoustic imaging devices to satisfy the thermal expansion condition, has a fundamentally low frame rate due to the low PRR (pulse repetition rate) problem. The developed receiving system consists of a single module that can transmit and receive US images, which has the advantage of using the low PPR of the Nd:YAG laser to receive PAM and USM (Ultrasound microscopy) images without lowering the frame rate taking advantage of these receiving systems, look forward to researching new application fields that combined PAM and USM images.

REFERENCES

1. Martí-Bonmatí, L.; Sopena, R.; Bartumeus, P.; Sopena, P. Multimodality imaging techniques. *Contrast Media Mol. Imaging* **2010**, *5*, 180–189, doi:10.1002/cmmi.393.
2. Powers, J.; Kremkau, F. Medical ultrasound systems. *Interface Focus* **2011**, *1*, 477–489, doi:10.1098/rsfs.2011.0027.
3. Jensen, J.A. Medical ultrasound imaging. *Prog. Biophys. Mol. Biol.* **2007**, *93*, 153–165, doi:10.1016/j.pbiomolbio.2006.07.025.
4. Hughes, S. Medical ultrasound imaging. *Phys. Educ.* **2001**, *36*, 468–475, doi:10.1088/0031-9120/36/6/304.
5. Kang, J.; Kim, E.K.; Young Kwak, J.; Yoo, Y.; Song, T.K.; Ho Chang, J. Optimal laser wavelength for photoacoustic imaging of breast microcalcifications. *Appl. Phys. Lett.* **2011**, *99*, 1–4, doi:10.1063/1.3651333.
6. Kim, H.; Lee, H.; Moon, H.; Kang, J.; Jang, Y.; Kim, D.; Kim, J.; Huynh, E.; Zheng, G.; Kim, H.; et al. Resonance-Based Frequency-Selective Amplification for Increased Photoacoustic Imaging Sensitivity. *ACS Photonics* **2019**, *6*, 2268–2276, doi:10.1021/acsphotonics.9b00576.
7. Moon, J.Y.; Lee, J.; Chang, J.H. Electrical impedance matching networks based on filter structures for high frequency ultrasound transducers. *Sensors Actuators, A Phys.* **2016**, *251*, 225–233, doi:10.1016/j.sna.2016.10.025.
8. Xing, W.; Wang, L.; Maslov, K.; Wang, L. V. Integrated optical- and acoustic-resolution photoacoustic microscopy based on an optical fiber bundle. *Opt. Lett.* **2013**, *38*, 52, doi:10.1364/ol.38.000052.
9. Park, S.; Kang, S.; Chang, J.H. Optically Transparent Focused Transducers for Combined Photoacoustic and Ultrasound Microscopy. *J. Med. Biol. Eng.* **2020**, *40*, 707–718, doi:10.1007/s40846-020-00536-5.
10. Liu, W.; Yao, J. Photoacoustic microscopy: principles and biomedical applications. *Biomed. Eng. Lett.* **2018**, *8*, 203–213, doi:10.1007/s13534-018-0067-2.
11. Schellenberg, M.W.; Hunt, H.K. Hand-held optoacoustic imaging: A review. *Photoacoustics* **2018**, *11*, 14–27, doi:10.1016/j.pacs.2018.07.001.
12. Chang, J.H.; Sun, L.; Yen, J.T.; Shung, K.K. Low-cost, high-speed back-end processing system for high-frequency ultrasound B-mode imaging. **2009**, *56*, 1490–1497.
13. Kurokawa, K. Design Theory of Balanced Transistor Amplifiers. *Bell Syst. Tech. J.* **1965**, *44*, 1675–1698, doi:10.1002/j.1538-7305.1965.tb04198.x.
14. Ieee, O.F.T.H.E. * I. **1964**.

15. Kim, H.; Jo, G.; Chang, J.H. Ultrasound-assisted photothermal therapy and real-time treatment monitoring. *Biomed. Opt. Express* **2018**, *9*, 4472, doi:10.1364/boe.9.004472.
16. Kim, J.; Kim, H.; Chang, J.H. Endoscopic probe for ultrasound-assisted photodynamic therapy of deep-lying tissue. *IEEE Access* **2020**, *8*, 179745–179753, doi:10.1109/ACCESS.2020.3026372.
17. Lee, J.; Chang, J.H. Dual-Element Intravascular Ultrasound Transducer for Tissue Harmonic Imaging and Frequency Compounding: Development and Imaging Performance Assessment. *IEEE Trans. Biomed. Eng.* **2019**, *66*, 3146–3155, doi:10.1109/TBME.2019.2901005.
18. Lee, J.; Member, S.; Shin, E.; Member, G.S. Development of Dual-Frequency Oblong-Shaped- Focused Transducers for Intravascular. **2018**, *65*, 1571–1582.
19. Kang, J.; Chang, J.H.; Kim, S.M.; Lee, H.J.; Kim, H.; Wilson, B.C.; Song, T.K. Real-time sentinel lymph node biopsy guidance using combined ultrasound, photoacoustic, fluorescence imaging: In vivo proof-of-principle and validation with nodal obstruction. *Sci. Rep.* **2017**, *7*, 1–9, doi:10.1038/srep45008.
20. Lee, J.; Jang, J.; Chang, J.H. Oblong-Shaped-Focused Transducers for Intravascular Ultrasound Imaging. *IEEE Trans. Biomed. Eng.* **2017**, *64*, 671–680, doi:10.1109/TBME.2016.2572182.

요 약 문

광 음향, 초음파 융합 영상을 위한 저잡음 광대역 수신 시스템 개발

광 음향 (Photoacoustic), 초음파 (Ultrasound) 융합 영상은 높은 공간 해상도 (Spatial resolution)와 높은 대조도 (Contrast resolution)의 영상을 제공하여 암과 같은 특정 질병 진단의 정확도를 향상시키는 영상을 제공한다. 일반적으로 광 음향 영상을 얻기 위하여 상용 초음파 영상 의료기기를 사용하게 된다. 그러나 상용 초음파 영상 의료기기는 상대적으로 낮은 주파수 대역폭과 샘플링의 제한으로 해부학적, 기능적 정보를 제공하는 광 음향 현미경 영상 (Photoacoustic microscopy)에서는 여러 상용 장비의 조합으로 구성된다. 여러 상용 장비를 거치면서 수신되는 광 음향 신호는 장비 간 임피던스 불일치로 인하여 신호의 감쇠와 잡음이 발생하는 문제가 생기며, 또한 장비 간 동기화 문제와 영상 깊이에 따라 수신 신호의 증폭도를 가변 할 수 없는 문제가 발생하여 영상의 신호 대 잡음 비 (Signal-to-Noise-Ratio; SNR), 대조도 (Contrast-to-Noise-Ratio; CNR) 성능을 저하시킨다. 이러한 문제를 해결하기 위해 본 논문은 광 음향, 초음파 융합 영상을 위한 저잡음 광대역 수신 시스템 개발과 평가, 결과에 관한 것이다. 개발한 저잡음 광대역 수신 시스템은 두 개의 저잡음 증폭기 (Low-noise amplifier), 두 개의 가변 이득 증폭기 (Variable gain amplifier), 아날로그 필터, 아날로그-디지털 변환기 (Analog-to-digital converter) 그리고 디지털 제어 로직으로 구성되어 있다. 개발한 시스템은 5 ~ 70 MHz 동작 주파수 대역에서 최대 76 dB의 증폭 이득과 48 dB의 가변 이득 범위를 만족하며, ±1 dB 증폭 이득 평탄도 성능을 가진다. 개발된 수신 시스템은 생체 모사 팬텀, 혈관 모사 팬텀, 와이어 타겟 팬텀 영상 실험을 통하여 상용 수신 시스템보다 6.7 dB 이상의 신호 대 잡음비 성능과 3 dB 이상의 대조도 성능이 우수함을 확인하였습니다.

핵심어: 광 음향 현미경; 대조도; 신호 대 잡음비; 저잡음 증폭기; 가변 이득 증폭기;